High Voltage Multijunction Photovoltaic Devices

Current Matching and the Characterization of Low Bandgap Material Germanium Tin

Thijs Blackstone

High Voltage Multijunction Photovoltaic Devices

Current Matching and the Characterization of Low Bandgap Material Germanium Tin

by

Thijs Blackstone

to obtain the degree of Master of Science
at the Delft University of Technology,
to be defended publicly on Monday August 15, 2022 at 15:00.

An electronic version of this thesis is available at `http://repository.tudelft.nl/`.

Preface

This thesis project challenged me in many ways. From learning and applying lab techniques and processes to sitting down day after day to write down my findings in a coherent and productive fashion. I am proud to see almost two years of work condensed into fifty pages of writing. I could not have done this by myself, so I wish to extend my sincerest gratitude to all those who have helped me along this journey.

First of all, I would like to thank the people of the PVMD group and of the EKL lab for their help and support during my thesis. In particular, I would like to thank my daily supervisor Thierry de Vrijer. His calm and patient demeanor was very pleasant, especially when I was stressed out about my project. His deep understanding of the material and his attention to detail helped me greatly in shaping my thesis.

I'd also like to thank prof. Arno Smets for his help and for supervising my thesis. His enthousiasm was contagious and he lightened the mood on many occasions. His dedication to the cause that photovoltaics support also shone through.

Furthermore, I would like to thank technicians Martijn Tijssen, Stefaan Heirman, and Daragh O'Connor for keeping all the equipment up and running and for helping me with all my machine related problems. They spent many hours fixing software, measurement machines and processing tools and I am grateful to them for it.

Furthermore, I'd like to thank Sander Miedema for working on many of the experimental runs together with me. I appreciate our time together in the lab during the covid lockdown, both socially and with regards to the work he and I did. Koos Roodenburg and Federica Saitta accompanied me during other experimental runs. I also want to thank them for sharing that work load and making it much more enjoyable.

Finally, I would like to thank Jade, my family and my friends for their unwavering support and belief in me. They helped me bear the rough days and celebrate the good days. From the bottom of my heart, thank you.

Thijs Blackstone
Delft, August 2022

Abstract

A next step in the energy transition is to produce green fuels from sunlight. One way to achieve this is via high voltage photovoltaic (PV) devices which can directly drive electrolysis reactions to produce hydrogen or other chemical fuels. Group IV based multijunction (MJ) PV devices are a candidate to function as these high voltage devices.

This work is focused on improving the efficiency of crystalline silicon/nano-crystalline silicon/amorphous silicon (c-Si/nc-Si/a-Si) triple junction (3J) solar cells through better current matching. On top of that, the low bandgap material germanium tin (GeSn:H) is characterized as it shows potential for use as bottom junction in multijunction photovoltaic devices.

Several methods were tried to improve current matching in the 3J PV devices. Varying the nc-Si middle absorber thickness was successful at improving the short-circuit current density (J_{sc}) in the middle junction, which was the current limiting junction. A range between 3-5µm nc-Si absorber thickness is effective at keeping the middle junction J_{sc} high while keeping open-circuit voltage (V_{oc}) and fill factor (FF) losses at an acceptable level. Varying the n-type nano-crystalline silicon oxide (n-nc-SiO$_x$) intermediate reflective layer (IRL) thickness was also effective at improving the J_{sc} of the middle junction. Introducing a silver IRL between the n-layer of the middle junction and the p-layer of the bottom junction was ineffective, as was introducing various transparent conductive oxides (TCOs). The J_{sc} of the middle junction did not increase with the introduction of these layers. In the case of the TCOs, the shunt resistance decreased drastically resulting in decreased V_{oc}s and FFs. The best performing device in this thesis was manufactured using a 400nm a-Si:H absorber, a 4.5µm i-nc-Si:H absorber and a 60nm n-nc-SiO$_x$ intermediate reflective layer. This device had a V_{oc} of 1.947V, FF of 0.789, a J_{sc} of 9.51mA/cm^2 and an efficiency of 14.6%, which, to the best of our knowledge, is the highest conversion efficiency achieved to date with this device architecture.

Introducing tetramethyltin (TMT) to process GeSn:H films resulted in carbonization of the films. Carbon passivates Ge dangling bonds better than hydrogen. This reduces the defect density, leading to higher activation energy (E_{act}) with high TMT injection rates. A high germane flow rate resulted in dense, relatively defect-free films with a high photoconductivity, low bandgap and near intrinsic semiconductor properties. A high germane flow of around 2 sccm is therefore recommended. Varying the pressure in the deposition chamber offers some control over post-processing oxidation, where higher pressure results in less oxidation. Changing the radiofrequency power offers a trade-off between film growth rate and film quality.

Contents

List of Figures

List of Tables

<div style="text-align: right">

1

</div>

Introduction

This chapter discusses the context for this thesis and by extension its relevance. Afterwards, the project is introduced in detail. Section 1.1 describes the global need for renewable energy and recent developments in the solar energy sector. In section 1.2 the DISCO project, of which this thesis is a part, is introduced and its purpose is explained. Finally, section 1.3 describes the goal of this thesis and outlines the structure of the rest of the document.

1.1. Global Climate and Energy Problem

Since the advent of the industrial revolution mankind has relied primarily on fossil fuels such as coal, oil and gas as its energy sources. Fossil fuels produce carbon dioxide (CO_2) when burned which leads to an increased CO_2 concentration in the atmosphere. CO_2 is great at absorbing infrared radiation, so increasing its concentration results in higher average temperatures on earth. This in turn leads to more extreme weather events and rising sea levels as the antarctic ice cap melts.
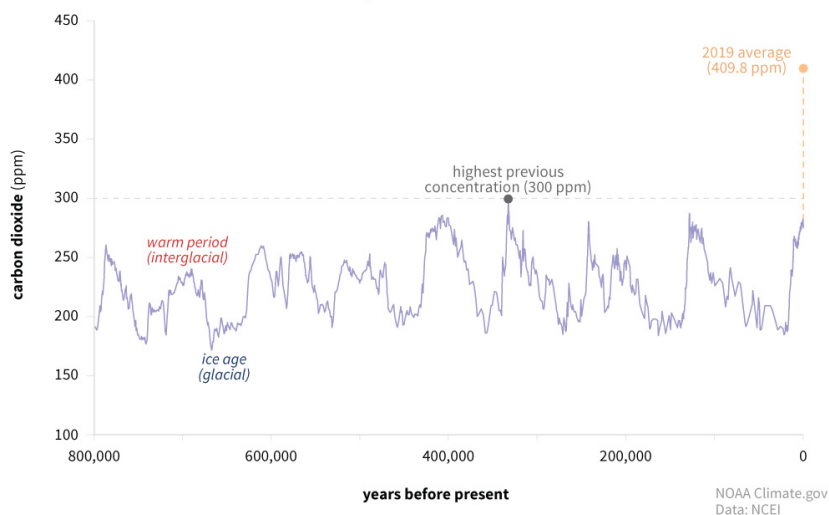
Figure 1.1: CO_2 concentration over geologic time scales. The near vertical upward line bordering the present is largely due to fossil fuel consumption since the industrial revolution. [26]

The rapidly increasing CO_2 concentration in the atmosphere calls for an energy transition towards renewable energy sources. As figure 1.2 shows, solar photovoltaic (PV) energy has fast become economically competitive. Solar PV was already on par with natural gas in terms of its levelized cost of

electricity (LCOE) in 2018. However, electricity accounts for only 20% of global energy consumption [9], which severely limits the scope of traditional electricity-producing solar cells. If solar cells could produce chemical fuels (called 'solar fuels') instead, their scope would increase up to five times. They could replace fossil fuels for functions such as transport, heating, cooking, and various industrial processes.
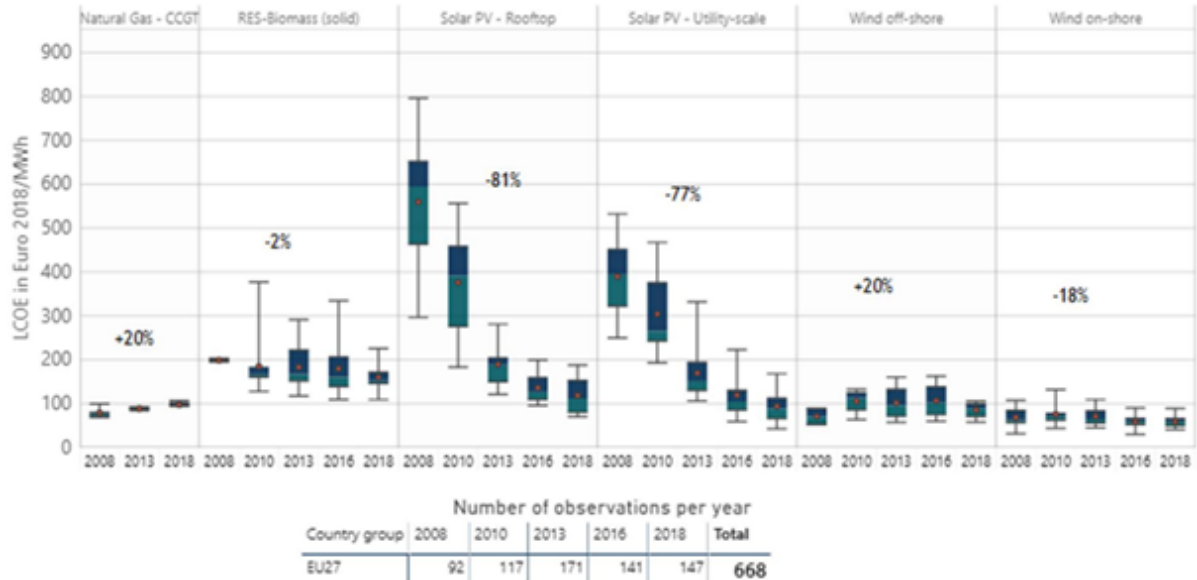
Figure 1.2: Levelized cost of electricity (LCOE) comparison of various energy sources between 2008-2018 [8].

1.2. DISCO Project

The DIrect Solar to CO conversion (DISCO) project aims to manufacture photovoltaic devices that can produce solar fuels. Sunlight is converted into electricity through a solar panel which powers the electrolysis of solar fuels. This process can be facilitated in many ways, as shown in figure 1.3.
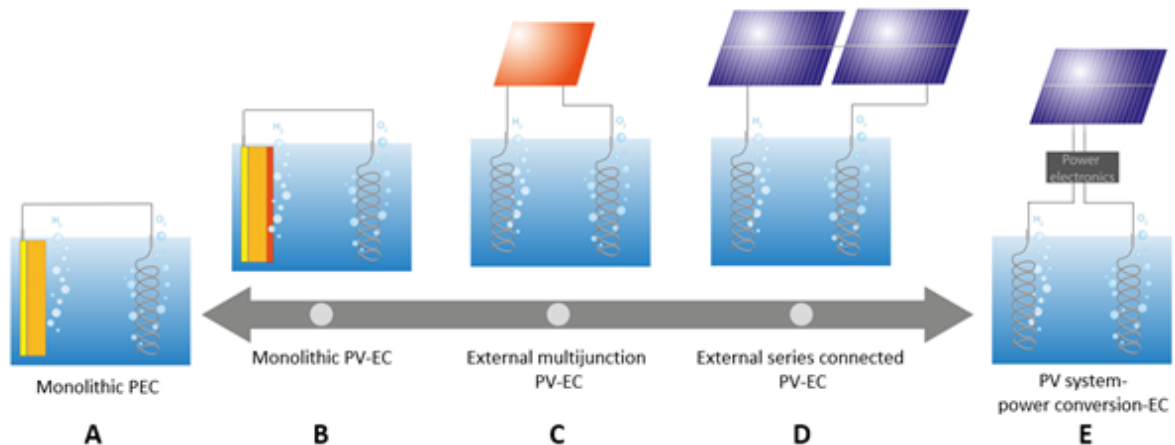
Figure 1.3: Different levels of integration of P(V)EC devices [30]. This figure shows a range of different ways to convert solar energy into chemical fuels. The level of integration decreases from left to right, from A) a completely integrated monolithic photo-electrochemical (PEC) device to E) a PV system that's connected to an electrolysis bath with an intermediary power electronics set-up that transforms the electricity generated by the solar cell into the right voltage for the desired electrolysis reaction. A) and B) place the solar cell inside the electrolysis bath. C) and D) place the solar cell outside the electrolysis bath and connect it via wires. E) adds power electronics to vary the voltage and current flowing to the electrolysis bath.

The DISCO project aims to generate the required voltage for the chemical reactions shown in figure 1.4 through the solar cell. Power electronics are therefore not required, eliminating design option E) from the equation. Work by Sander Miedema [27] and Mohammed El Makkaoui [12] investigated options A) and B) by looking at the effects of introducing pores into the solar cell to speed up the electrolysis reaction. This thesis focuses on the performance of the solar cell.
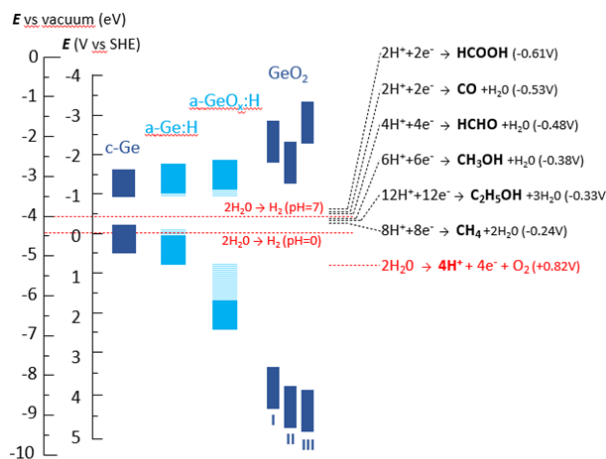
Figure 1.4: Voltage required for specific electrolysis reactions. All end products (CO, CH_4, HCOOH, HCHO, CH_5OH, and C_2H_5OH) can be used as chemical fuels.

Electrolysis requires a minimum voltage to occur which depends on the electrolysis reaction in question. Figure 1.4 illustrates a range of compounds and the required voltage to produce them via electrolysis. The theoretical voltage required is the voltage difference between the (red) water splitting reaction and the product. In practice, there are always losses. Therefore, the aim is to optimize a solar cell with a minimum open-circuit voltage (V_{oc}) of 2V.
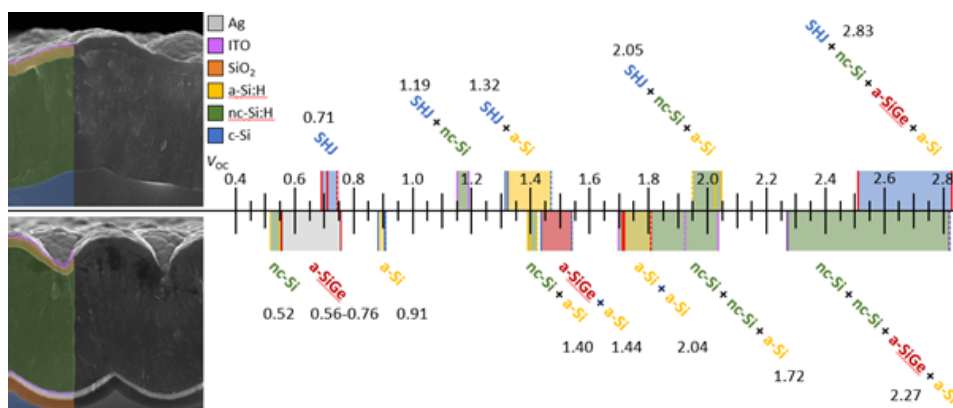
Figure 1.5: Open-circuit voltage (V_{oc}) range of different single- and multijunction PV device architectures. The upper row shows silicon hetero-junction (SHJ) and hybrid SHJ plus thin film silicon (SHJ+) multijunction devices. The layers are written in order from bottom to top cell, e.g. 'SHJ + nc-Si + a-Si´ has a SHJ bottom cell, an nc-Si middle cell and an a-Si top cell. The top cell comes into contact with incoming light first. The lower row shows thin film silicon devices. These devices use a silicon wafer to transfer surface textures onto the thin films, and are electrically separated from the thin films by a layer of silicon dioxide. On the left of the figure, coloured scanning electron microscope (SEM) images of the cross-section of both types of devices are shown. Each colour corresponds to a specific material as labeled by the legend. There are three lines for every architecture. The solid lines represent the highest measured V_{oc} (of which the V_{oc} is presented above/below the architecture) and the V_{oc} of the device with the highest V_{oc}*FF product that are produced in the EKL lab. The dashed line is the V_{oc} of the device with the highest reported conversion efficiency for that architecture. Some architectures do not have this dashed line, because these architectures have not been reported in literature yet.

Figure 1.5 shows several device architectures and their voltage ranges. A high voltage can be achieved by stacking multiple semiconductors with different bandgap energies on top of each other

and integrating them into a single device, as shown in figure 1.5. To reach the desired V_{oc} of 2V requires at least three junctions. One such architecture is a crystalline silicon (c-Si) - nanocrystalline silicon (nc-Si) - amorphous silicon (a-Si) device, which can currently reach voltages up to 2.05V as shown in figure 1.5. Because a high voltage is a design requirement, a 2-terminal design is chosen. A 3-terminal (or any amount of terminals above 2) design causes junctions to be electrically connected in parallel, which limits the voltage of the device to the voltage of the cell with the lowest voltage [42]. In a 2-terminal architecture, the voltages stack when the junctions are connected in series.

There are plenty of reasons to use group 4 elements, and silicon in particular, in solar cells. One reason is group 4 elements' great chemical stability. Another reason is silicon's relative abundance on Earth's surface, making it cheap compared alternatives like germanium and tin. This contrast is even more apparent in other materials like gallium and selenium used in chalcogenide solar cells. The decision to stack the junctions of the multijunction device monolithically was made for two reasons: the complete device can be processed on a single substrate and the process is far simpler than for mechanically stacked or spectrum-split devices [42].

1.3. Project Description and Outline

Many theses have already been completed as part of the DISCO project. These were focused on developing new absorber materials [5] [33] [34], optimising the photovoltaic stack [3] [29] [28] [27], developing new surface texturing [28] and investigating pores for a photoelectrochemical device [12]. This thesis builds on their work.

The overarching research goal of this thesis is to manufacture multijunction solar cells with a wide range of output voltages to produce various solar fuels. To achieve this, two sub-goals are formulated:

1. To increase the conversion efficiency of c-Si/nc-Si/a-Si devices through improved current matching

2. To characterize low bandgap material germanium tin for use as bottom junction in multijunction PV devices

This thesis is organized as follows: Chapter 2 discusses the relevant theory, including photovoltaic fundamentals and multijunction solar cell theory. Chapter 3 details the processes to produce solar cells in the lab and which tools are used to do so. Chapter 4 goes into the measurement equipment. Chapter 5 presents the results of the multijunction current matching experiments and interprets their meaning. Chapter 6 does so for the germanium tin characterization experiments. Chapter 7 gives conclusions and makes recommendations for future research.

2

Theoretical Background

The goal of this thesis is to develop a solar cell that can be integrated into an autonomous device that produces solar fuels. To achieve this, multijunction photovoltaic devices are used. In order to understand how these devices work, this chapter discusses the fundamental concepts of photovoltaics. These concepts include solar radiation, semiconductor physics, loss mechanisms, optics and light management, and material properties. The fundamental concepts are then used to explain multijunction cells and photoelectrochemical devices. Finally, solar cell parameters are discussed. Solar cell parameters are crucial to the characterization and measurement of solar cells.

2.1. Photovoltaic Fundamentals

Devices that convert solar energy into electricity using semiconductor materials are called photovoltaic (PV) devices.

2.1.1. Solar Radiation
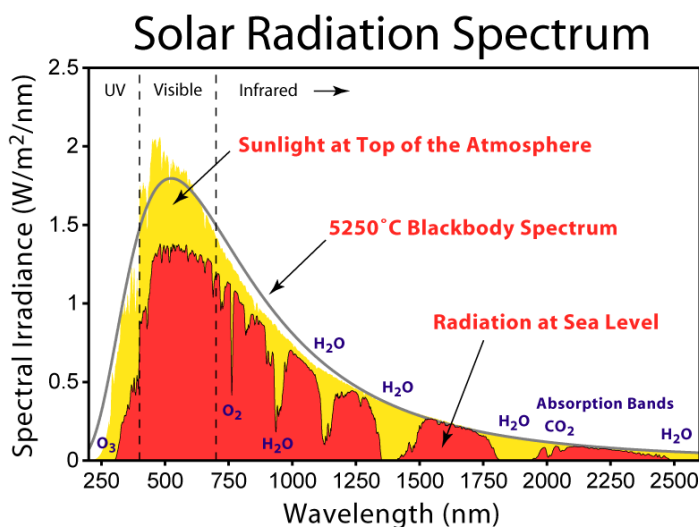
Figure 2.1: The solar spectrum. This image shows the spectral irradiance of the sun in W/m^2/nm plotted against the wavelength of emitted light in nm. The yellow area indicates the solar spectrum just outside Earth's atmosphere. The red area indicates the solar spectrum at sea level. The black line shows the spectral irradiance of a black body at 5250 °C. [41]

Figure 2.1 shows the spectral irradiance of the sun. The spectral irradiance peaks around 500nm with significant irradiance between 300-900 nm. This is therefore the region where the most energy is to be harvested. Light can be described as consisting of well defined energy packets called photons. The energy of a photon is given by equation 2.1:

$$E = hf \tag{2.1}$$

where h is Planck's constant ($6.626 * 10^{-34} \frac{m^2 kg}{s}$) and f is the frequency of the photon. This characterization of photons is relevant to describe how sunlight is captured and converted into electricity in solar cells through semiconductors.

2.1.2. Semiconductor Physics

A material can absorb photons by using the energy of the photon to excite an electron into a higher energy band. In principle, this only happens when the energy of the absorbed photon is at least equal to the difference in energy between the two energy bands.

$$hf = E_c - E_v \geq E_g \tag{2.2}$$

Where E_c is the energy level of the conduction band edge, E_v is the energy level of the valence band edge, and E_g is the bandgap energy. The relative energy levels of valence and conduction bands are specific to the material at hand. As shown in figure 2.2a, energy bands in metals (conductors) overlap, resulting in a sea of electrons that move about freely. This makes metals very useful to conduct electricity. On the other hand, insulators have a large bandgap energy, preventing the movement of charge carriers.
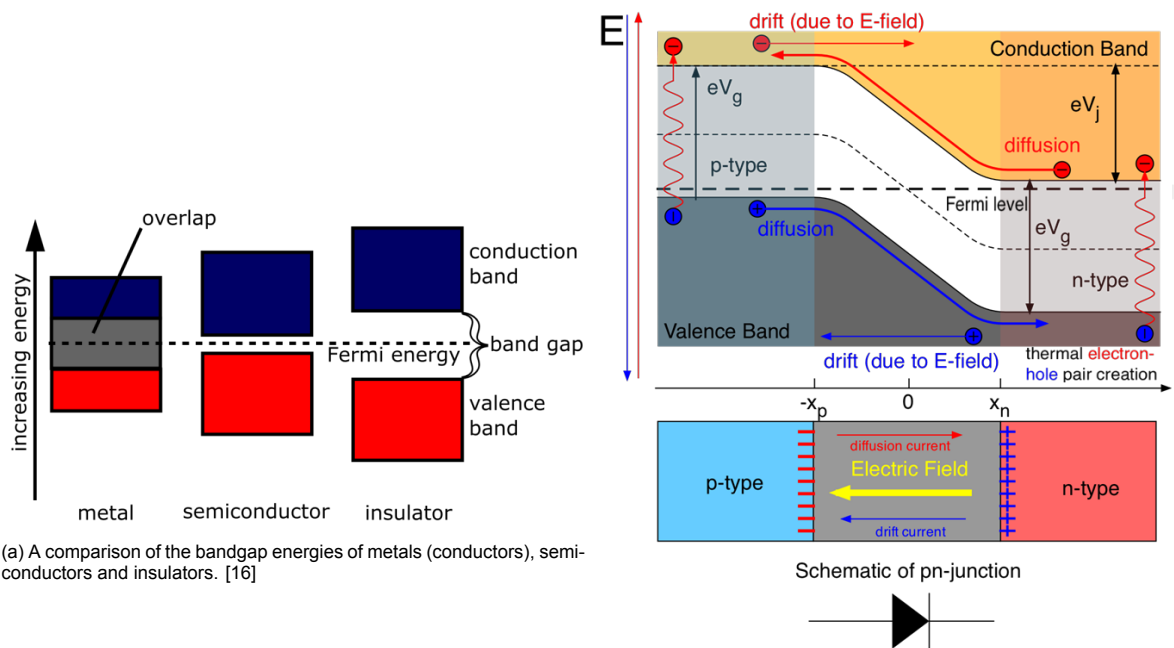
(a) A comparison of the bandgap energies of metals (conductors), semiconductors and insulators. [16]

(b) A schematic of a pn-junction [31]. The Fermi level is close to the valence band edge in the p-type material (left) whereas the Fermi level is close to the conduction band edge in the n-type material (right). If the material were intrinsic, the Fermi level would be on the dotted line midway between the valence and conduction band edges.

Figure 2.2: bandgap comparison and the use of pn-junctions to create a diode.

Semiconductors have bandgap energies between those of metals and insulators, making them extremely useful for solar cells. The optimal bandgap energy for a single junction solar cell to capture the most solar energy is 1.4 electronvolt (eV) [46] [35]. The bandgap energy of crystalline silicon (c-Si) is 1.1 eV. This is sub-optimal, but its high stability and abundance contribute to make c-Si the most used semiconductor for solar panels to date.

When an electron is excited, it leaves behind something called a hole. This is a positive 'particle´ that can move through the material by swapping places with nearby electrons. When an electron is excited, what is created is an electron-hole pair. In short, the radiative energy of the photon is transformed into the chemical energy of an electron-hole pair. This chemical energy can then be used to power an electric circuit. In solar cells, pn-junctions are used to separate electron-hole pairs before they recombine and their energy is lost. The following paragraphs will explain pn-junctions.

Doping is of crucial importance in solar cells. Doping occurs when atoms with either more or less valence electrons than the bulk material are introduced into that material. Considering silicon as bulk material (with four valence electrons), boron would be a p-type dopant. Boron has three valence electrons, so compared to the surrounding silicon atoms it carries an additional positively charged hole. A common n-type dopant for silicon is phosphorus as it has five valence electrons.

Bringing together a p-type and n-type material creates a pn-junction. The difference in electrical charge creates an electric field. This electric field is the driving factor for drift as shown in figure 2.2b. Furthermore, diffusion caused by the concentration gradient of holes and electrons at the pn-junction results in a depletion region. The depletion region is an area at the interface of the p- and n-type materials where there is no net charge. This depletion region blocks the flow of electrons from the n-side to the p-side of the semiconductor diode while allowing flow in the opposite direction, essentially creating a diode.

2.1.3. Loss Mechanisms

The efficiency of a solar cell is limited by fundamental loss mechanisms, as well as practical production limits. Some loss mechanisms that play a large role in this research are parasitic absorption and some forms of recombination. Recombination occurs when an electron-hole pair recombines before reaching the p- and n-type contacts to travel through the external circuit. Electron-hole pairs have a lifetime: the average time before they recombine. In that time, the charge carriers must reach the p- and n-type contacts. This implies that increasing the absorber layer thickness increases recombination losses. Charge carriers have to travel further and for a longer time to reach the p- and n-type contacts which increases the odds that they come into contact with each other (electrons with holes and vice versa) and recombine.

The inability to convert photons below the bandgap energy level into electricity is one loss mechanism. Thermalization of photons with an energy that exceeds the bandgap energy is another loss mechanism. Thermalization basically converts any energy in excess of the bandgap energy into kinetic energy which heats up the material. Taking these loss mechanisms into account, the Shockley-Queisser efficiency limit was calculated to be 30% in 1961 for a material with a bandgap of 1.1 eV [37]. This limit has later been recalculated to take other loss mechanisms into account [32]. Mainly Auger recombination has a big impact on c-Si solar cells. The recalculated limit stands at 29.43% [32].

2.1.4. Optics and Light Management

Figure 2.3 traces light entering a silicon cell with sharp pyramid texturing. It can be seen that the pyramids serve multiple purposes. Firstly, the light has multiple chances to pass through the air-silicon interface as it interacts with the surface multiple times. This increases the amount of light that is transmitted through the air-silicon interface into the silicon. Secondly, the pyramids cause the light to enter the solar cell at an angle, which increases the distance the light travels through the solar cell (the path length). This results in a higher chance that the light excites an electron to create an electron-hole pair. The other surface textures that are used in this thesis, such as honeycombs or smooth pyramids, also serve these three purposes.
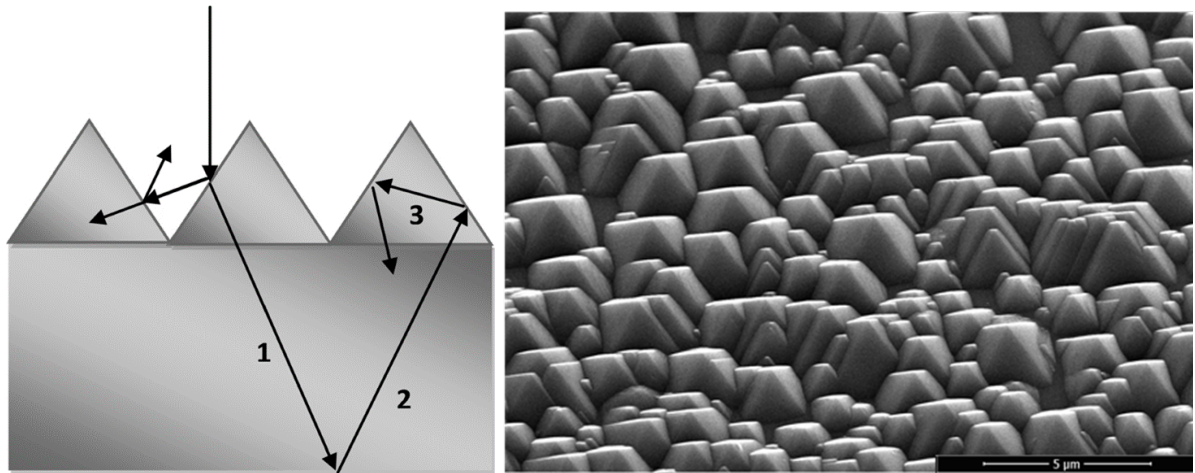
Figure 2.3: Left: Schematic diagram of reflection and transmission for an air-silicon interface with sharp pyramid texturing [20]. Right: Scanning electron microscope (SEM) image of sharp pyramid texture.

2.2. Solar Cell Materials

Different semiconductor materials have different bandgap energies. They can be combined into multijunction devices to capture a large portion of the solar spectrum while simultaneously allowing for a range of output voltages. There are several materials that are of interest in this thesis, which are discussed below.

2.2.1. Silicon

Silicon has a few morphologies which differ in their bandgap energies. The three that are used in this thesis are crystalline silicon (c-Si), nanocrystalline silicon (nc-Si) and amorphous silicon (a-Si). c-Si (figure 2.4a left) is a form of silicon in which each silicon atom is bonded to four other silicon atoms. c-Si has a long range crystal structure. It has an indirect bandgap energy of 1.12 eV.
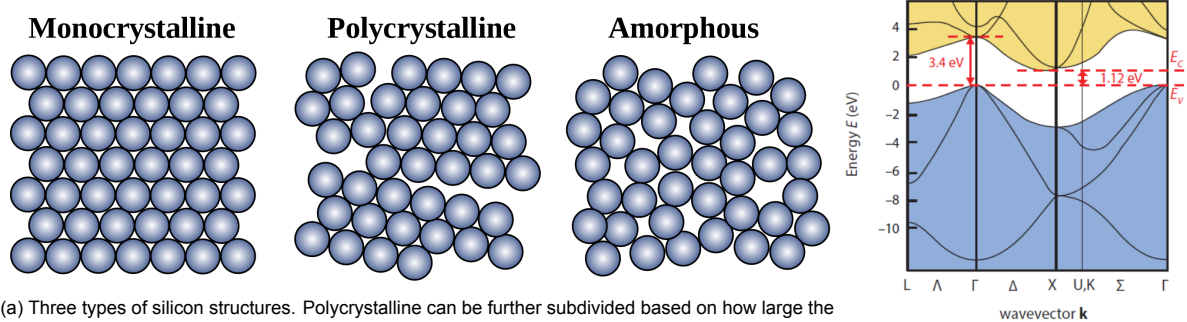
(a) Three types of silicon structures. Polycrystalline can be further subdivided based on how large the crystals are. [1]

(b) The band diagram of crystalline silicon.

Figure 2.4: Silicon morphologies and the band diagram of c-Si.

A bandgap is direct when an electron can be excited from the valence band to the conduction band without exchanging momentum with the lattice. A bandgap is indirect when such a momentum exchange is necessary for the electron to be excited to the conduction band. The absorption coefficient of direct bandgap materials is much higher than that of indirect bandgap materials. This has a direct impact on how thick the absorber must be. Materials with an indirect bandgap require thicker absorber layers than direct bandgap materials in order to absorb a similar amount of light.

Figure 2.4b shows that crystalline silicon has an indirect bandgap energy of 1.12 eV and therefore

requires momentum in the form of a phonon to excite an electron to the conduction band when absorbing a photon with an energy between 1.12-3.4 eV [39]. Any photon with energy excess of 3.4 eV can be absorbed directly by c-Si.

Polycrystalline silicon (figure 2.4a middle) is a form of silicon that occurs when its crystal lattice has multiple grains with different orientations and boundaries between the grains. Nanocrystalline silicon is slightly different, as it consists of many small crystalline silicon grains with amorphous silicon between the grains: it has both an amorphous phase and a crystalline phase. For nc-Si, these smaller crystals are in the nanometer scale. The amorphous phase has a higher bandgap energy than the crystalline phase. The degree of crystallinity affects the average bandgap energy of the material. The more crystalline, the lower the average bandgap energy.

a-Si (figure 2.4a right) is a form of silicon which lacks long range order in its structure. This type of silicon has the highest bandgap of the three discussed in this paper, around 1.8 eV [24]. Furthermore, the bandgap of of a-Si is direct as opposed to the indirect bandgap of c-Si.

2.2.2. Germanium Tin

Germanium tin (GeSn) is a material which could have an even lower bandgap energy than c-Si. This is of interest, because it allows for more precise manipulation of the device voltage. Furthermore, it enables the capture of low-energy photons in the infrared range. Hydrogenated germanium (Ge:H) has a bandgap of 1.0 eV [23]. Hydrogenated germaniun tin (GeSn:H) has a bandgap between 0.4-1.0 eV [21], depending on the relative concentrations of germanium and tin. Chapter 6 dives into material property research on GeSn:H to assess its viability in multijunction PV devices.

2.3. Multijunction Solar Cells

Stacking junctions leads to the creation of a multijunction (MJ) cell. The junctions are placed in order of the bandgap energies of their absorber layers. The junction with the highest absorber layer bandgap energy is placed directly below the top contact of the MJ device and is therefore called the top junction. The middle junction is placed beneath the top junction and its absorber layer has a bandgap energy in-between that of the top and bottom junction absorber layers. The bottom junction has the absorber layer with the lowest bandgap and is placed directly above the bottom contact. An all-silicon triple junction solar cell would be ordered c-Si/nc-Si/a-Si from bottom to top, as shown in figure 3.5.

The reasons behind an all-silicon device are twofold. Firstly, silicon is abundant on earth and therefore relatively cheap. Secondly, silicon's bandgap aligns well with the solar spectrum. Having chosen to work with silicon, it becomes clear that a multijunction device is necessary. The bandgap of silicon (1.12 eV) is lower than the minimum voltage required to electrolyse hydrogen from water, 1.48V [17]. In practice, there are multiple causes for voltage loss in MJ devices, so an overpotential is necessary. In this thesis, the desired voltage is 2V. In a monolithically integrated MJ cell, the device voltage is equal to the sum of the voltage of each junction minus losses as illustrated by figure 1.5. Using multiple junctions also makes it possible to collect a larger part of the solar spectrum effectively. The high bandgap materials (a-Si:H, a-SiO$_x$:H) collect high energy photons with less thermalization losses, while the low bandgap materials (a-GeSn:H, c-Si) collect low energy photons.

Tunnel recombination junctions (TRJ) are essential in MJ cells. A TRJ is a pn-junction that functions as a charge collector between absorber layers. Without a TRJ, the n-layer of the top junction and p-layer of the middle junction would be in direct contact, which would create a pn-junction with an opposing electric in relation to the electric fields created by the pn-junctions of the top, middle and bottom cells. This is also the case between the middle and bottom junctions. This would ultimately lead to a lower V$_{oc}$ and FF. The ideal TRJ is an ohmic contact with non-rectifying behaviour [11].

Another critical aspect of MJ cells is current matching. The device will operate at the current of the junction with the lowest current [4]. This junction is called the 'current limiting junction'. Increasing

alloy	Band gap (eV)
a-GeSn:H	0.6-1.0
c-Si	1.1
nc-Si:H	1.1-1.3
a-Si:H	1.6-1.8
a-SiOx:H	>2.0
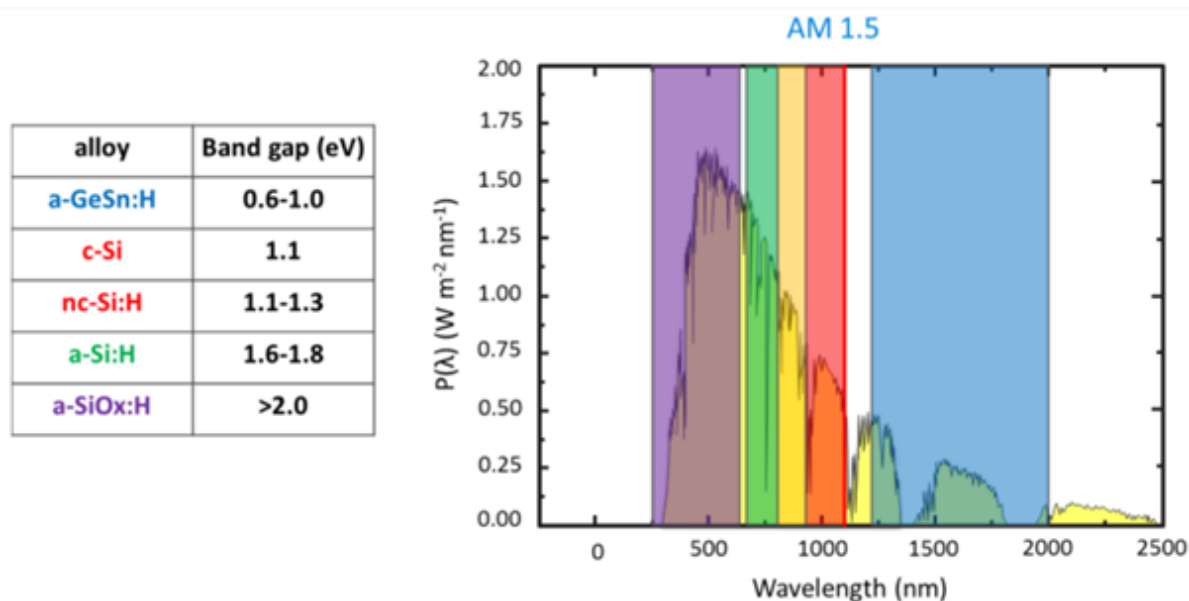
Figure 2.5: bandgap ranges for some group IV alloys [34]. Combining multiple of these alloys into an MJ device allows for more efficient conversion of a large portion of the solar spectrum.

the current in this junction improves the performance of the device as a whole. In this thesis, several approaches are taken to do so, including changing absorber layer thicknesses and introducing intermediate reflective layers (IRLs). The results are discussed in chapter 5.

IRLs are placed at the interface of two junctions, for instance the middle and bottom junctions, with the aim to reflect light back into the middle junction. The IRL would increase the path length of the light through the middle junction, resulting in a higher chance of absorption in the absorber layer of the middle junction, which would increase the current density in the middle junction. This increased current density in the middle junction comes at the cost of a decreased current density in the bottom junction due to the fact that less photons enter the bottom junction. If the middle junction is current limiting, 'redistributing' current from the bottom junction to the middle junction via an IRL may be worthwhile.

2.4. Photoelectrochemical Devices

Photoelectrochemical (PEC) devices convert sunlight directly into chemical fuels. The products of PEC devices are referred to as solar fuels. Two major advantages to PEC devices are the reduction in conversion steps and the level of integration. For example, the elimination of power electronics in the device reduces electronic losses and the amount of components. The integration of the device is especially useful for autonomous devices in remote locations. There are different levels of integration of PEC devices, as shown in figure 2.6.

This thesis focuses on the optimization of the PV part of these design architectures. The necessary voltage to drive the electrolysis reaction will be delivered by the solar cell, so the cells produced for this thesis could be used in set-ups A through D in figure 2.6. The minimum necessary voltage to split water is 1.48V [17]. Because there will be voltage losses in the solar cell and the external circuit, the aim of this paper is to optimize MJ cells with a V_{oc} of 2V or higher. There are also other reactions that are of interest, like the electrolysis of formic acid, but those are beyond the scope of this thesis.

2.5. Solar Cell Parameters

In order to understand and interpret the results shown in the following chapters, an understanding of solar cell parameters is required. There are several important parameters that are used to characterize
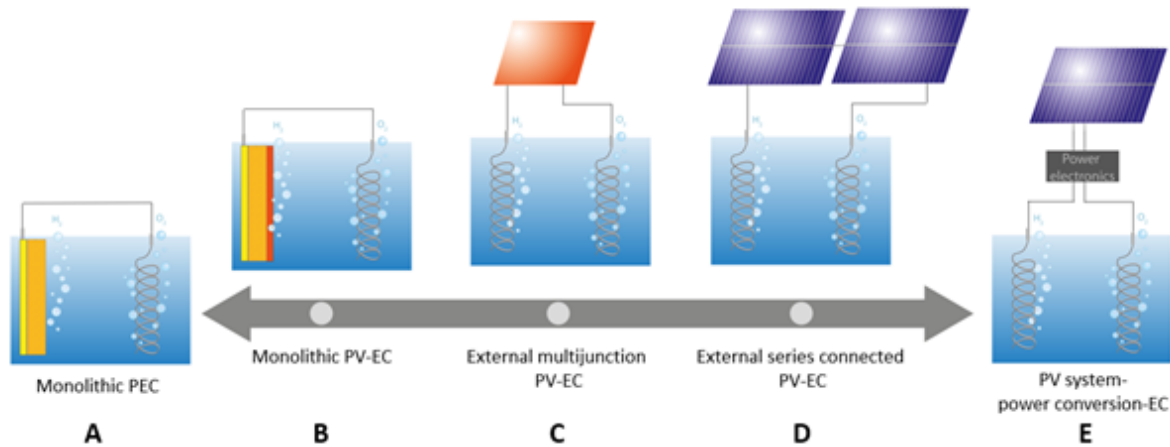
Figure 2.6: Different levels of integration of P(V)EC devices [30]. This figure shows a range of different ways to convert solar energy into chemical fuels. The level of integration decreases from left to right, from A) a completely integrated monolithic PEC device to E) a PV system that's connected to an electrolysis bath with an intermediary power electronics set-up that transforms the electricity generated by the solar cell into the right voltage for the desired electrolysis reaction. A) and B) place the solar cell inside the electrolysis bath. C) and D) place the solar cell outside the electrolysis bath and connect it via wires. E) adds power electronics to vary the voltage and current flowing to the electrolysis bath.

solar cells. These include the open-circuit voltage (V_{oc}), short-circuit current (J_{sc}), fill factor (FF), and efficiency.
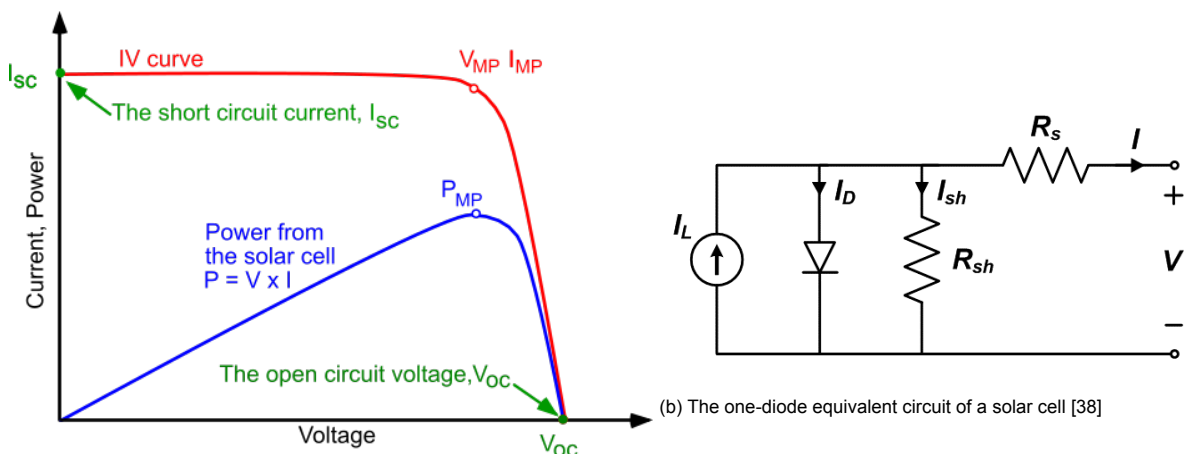
(a) A JV Curve [18]. In this graph, I stands for current. The rest of this thesis uses J for current.

(b) The one-diode equivalent circuit of a solar cell [38]

Figure 2.7: Schematics about solar cell parameters

The open-circuit voltage, V_{oc}, of a cell is the voltage between the front and back contact when the circuit is 'open': when no current flows through the circuit. The short-circuit current, J_{sc}, of a cell is the current that flows through the circuit when the circuit is shorted: when there is no voltage difference between the terminals. The fill factor, FF, of a solar cell is calculated using the following formula:

$$FF = \frac{P_{mpp}}{J_{sc} * V_{oc}} \tag{2.3}$$

where P_{mpp} is the power of the solar cell at the maximum power point (mpp), the highest power which the solar cell can generate. The efficiency of a solar cell is defined as the ratio of output power to input power:

$$Eff = \frac{P_{out}}{P_{in}} \tag{2.4}$$

R_s is the series resistance of a solar cell. R_{sh} is the shunt resistance. In general, the higher R_{sh} the better, because the current flowing through R_{sh} (I_{sh}) cannot be utilized by the load. A low R_s is desirable, because the lower R_s is, the larger the percentage of total current that will flow through the load.

3

Fabrication

This chapter discusses fabrication methods for both the multijunction (MJ) devices and the germanium-tin (GeSn) films. The processes to create MJ devices and GeSn films are described alongside the machines which are used for processing. First, a short introduction on MJ devices is given, after which each process is explained in more detail.
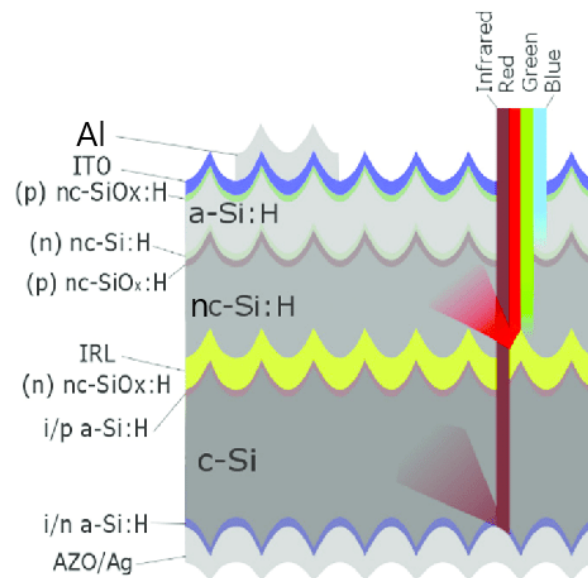
Figure 3.1: Triple junction solar stack. All layers other than the c-Si layer are made in-house. [22]

Figure 3.1 shows the layers of a triple junction solar cell. The crystalline silicon (c-Si) wafer is produced commercially by Topsil and consists of a 280±20μm n-type double side polished crystalline silicon wafer with a 1-0-0 crystal orientation and a lifetime of over 2000 microseconds. All other layers are deposited on-site. There are several different processes which are required to deposit these layers.

Firstly, the surface texture is etched into the silicon wafer. Secondly, the wafer is cleaned. Then, plasma enhanced chemical vapor deposition (PECVD) is used to deposit the photoactive stack, followed by sputtering and finally evaporation for transparent conductive oxide (TCO) layers and the metal contacts respectively. These steps will be discussed in chronological processing order as shown in figure 3.2.
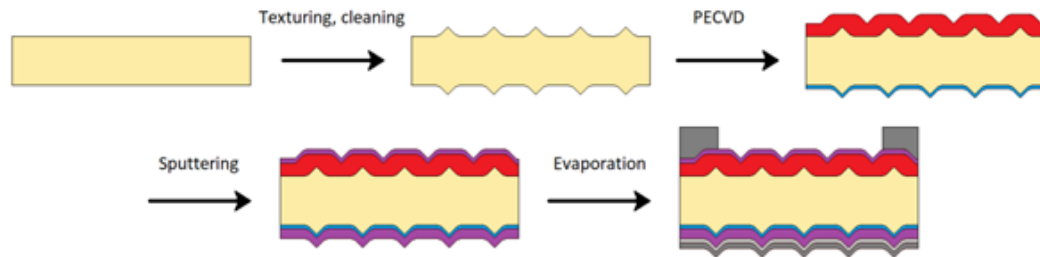
Figure 3.2: Multijunction cell processing order. Beige indicates the silicon wafer, red the p-layer stack, blue the n-layer stack, purple the ITO layer, light grey indicates silver and chromium, and finally dark grey is aluminium. [27]

3.1. Surface Texture

Before any depositions of photoactive layers occur, the surface pattern must be created. The surface texture serves the function of increasing the amount of light that is absorbed by the solar cell. There are two different textures that are used in this research.

3.1.1. Smooth Pyramids

A simple way to absorb more light is to use a sharp pyramid texture. This causes incoming light to come into contact with the surface of the solar cell multiple times, increasing the amount of reflection events and thereby the percentage of light that is coupled into the device. Sharp pyramids also cause photons to enter the device at an angle, increasing their path length through the device, which results in a higher chance that they are absorbed. It is important to note that these two features are not unique to sharp pyramids. Many different surface textures share these features. A problem with sharp pyramids is that some of the thin film layers that are deposited on top of them, particularly nano- and poly-crystalline layers, crack [28] due to the sharpness of the peaks. This ruins the performance of the device and is therefore not an option. An alternative is to use smoothened pyramids, which are less sharp while also having smaller peaks and troughs as can be seen in Figure 3.3. Smoothened pyramids are the first of the two textures in this thesis.

There are two main steps involved in making a smooth pyramid surface texture. First, a silicon wafer is wet etched by submerging it in a bath filled with a 1:5 ratio of tetramethyl ammonium hydroxide (TMAH):H_2O alongside 120mL of GP Solar surfactant fluid for around fifteen minutes. This mixture etches silicon anisotropically, changing the surface texture from a <100> orientation to a <111> orientation, thereby creating a sharp pyramid surface texture (Figure 3.3 left). The wafers are then rinsed in a bath filled with DI water for 5 minutes and dried with a nitrogen gun. Afterwards, another etching step occurs. A polysilicon etch mixture is used consisting of 3:1:6 HNO_3:HF:H_2O for 6 minutes. This mixture etches the silicon isotropically, smoothening out the pyramids (Figure 3.3 right).
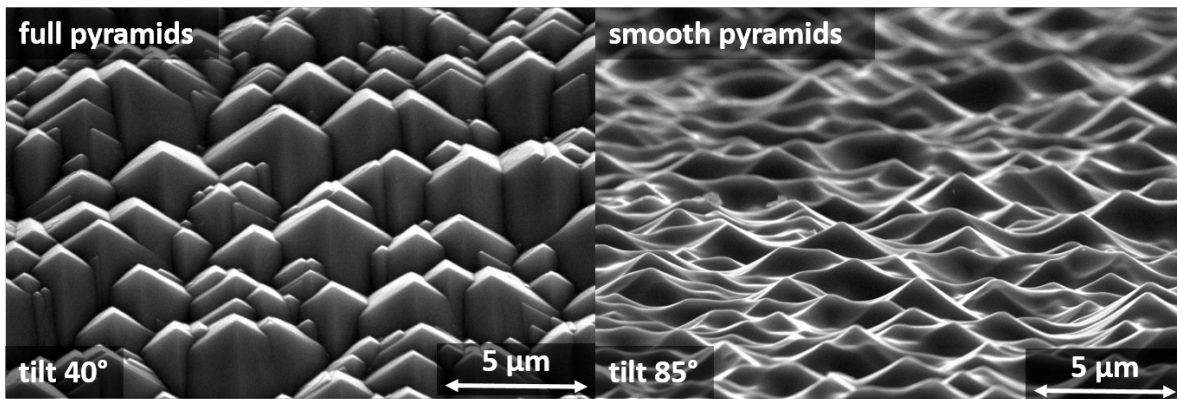
Figure 3.3: SEM image of sharp pyramid (<111>) texture on the left and smooth pyramid (between <100> and <111>) on the right. [28]

3.1.2. Honeycombs

The second surface texture used in this thesis is called a honeycomb texture. The term honeycomb is used, because the hexagonal pattern resembles a honeycomb (see Figure 3.4b). Research has shown that a honeycomb surface texture enhances both the J_{sc} and efficiency in thin-film microcrystalline silicon solar cells [36]. Figure 3.4a is a visual representation of the process that is used to create a honeycomb pattern.
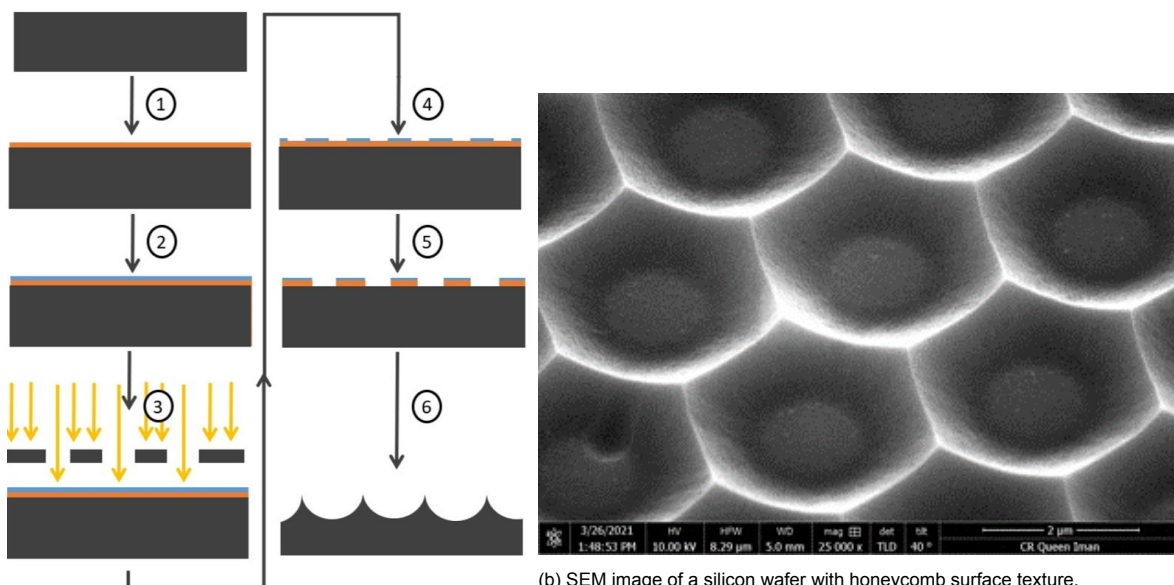
(b) SEM image of a silicon wafer with honeycomb surface texture.

(a) Visual representation of the steps to create a honeycomb structure. The silicon wafer is black. The orange layer represents the SiO_2 layer. Grey means photoresist. [28]

Figure 3.4: The process to produce a honeycomb surface texture and an SEM image of a honeycomb.

First, the silicon wafer is cleaned in a 0.55% HF bath for four minutes in order to remove any native oxide and plastic particles contained therein. After four minutes, the wafer is rinsed with DI water until the resistivity is 5MΩ, after which it is dried. Immediately following this cleaning process, a small layer of silicon is oxidized into a layer of silicon dioxide (SiO_2) 300nm thick in a furnace using wet oxidation with nitrogen and oxygen at 1100 °C for 16 minutes. This SiO_2 serves as a mask to protect parts of the silicon wafer from being etched away later on in the process. 300nm is chosen, because this is the minimum necessary thickness to completely protect the backside of the wafer from being etched away by the polysilicon etch.

Now that the protective SiO_2 layer is in place, it is time to pattern its surface. This is done in three steps. First, a coating of positive photoresist is applied on the front side of the wafer using an EVG120 coater/developer. Second, a pattern of circles 1 micrometer in diameter and 3 micrometers apart (center to center) is exposed onto the photoresist using an ASML PAS5500/80 automatic wafer stepper. Third, the sample is developed using the same EVG 120 coater/developer. During this step, the photoresist is hardened on unexposed area, while it is removed on any exposed area. Now that the pattern is present on the photoresist, it is time to transfer it to the SiO_2 layer. This is done using a dry oxidation process which etches SiO_2, but does not etch photoresist. After the full 300nm of silicon dioxide is removed, the remaining photoresist is evaporated in an acetone bath for one minute. This step is omitted from Figure 3.4a. Now, the pattern of circles has been transferred to the SiO_2 layer.

To finish the process, the silicon underneath the SiO_2 layer is etched away to form the honeycombs. However, the wafer must first be cleaned. This is done using a succession of different baths. It is important to let any remaining acetone evaporate before cleaning the wafer, as acetone explodes when it comes into contact with nitric acid. First, the samples are submerged in a 99% HNO_3 bath at 25°C for 10 minutes. The samples are rinsed in DI water before being placed in the next bath of 69.5% HNO_3 at 110 °C for another 10 minutes. The samples are rinsed again and then dried. Now they are ready to be etched. A polysilicon etch solution consisting of 35:14:1 HNO_3 (69.5%):H_2O:HF (40%) is prepared. Previous research has shown that etching should be done in steps to avoid etching reactants accumulating inside the holes of the silicon dioxide mask, which would lead to a reduction of the etching rate in silicon [45]. The steps are: 5 minutes of etching followed by 5 minutes of rinsing in water. Again 5 minutes of etching followed by 5 minutes of rinsing in water. Finally, 2 minutes of etching followed by 5 minutes of rinsing. At this point the honeycomb texture has been created in the silicon wafer. The final steps consist of another round of rinsing and drying, the removal of any remaining silicon dioxide using a buffered HF (BHF) etch solution, and finally a last round of rinsing and drying.

3.2. Wafer Cleaning

Before the wafers are ready to be processed with layer depositions, they must be cleaned. This is done in the cleaning line in a similar fashion as with the honeycomb production. The wafers are submerged in a bath of 99% HNO_3 solution at room temperature for ten minutes. Directly afterwards, the wafers are rinsed in a water bath until the resistivity of the wafers is 5MΩ. After this, the wafers are submerged in another bath containing 69.5% HNO_3 at 110°C for ten minutes. Again, the wafers are rinsed afterwards until their resistivity is 5MΩ. Next, the wafers are dried using the 'Avenger Ultra-Pure 6' rinser/dryer machine. Finally, the wafers are submerged in a 0,55% HF bath for 4 minutes (and rinsed/dried again) to remove any silicon dioxide deposits on the wafer. This whole process is performed a total of three times to ensure optimal cleanliness. One important caveat is that, the third time, the wafers do not get the 0,55% HF treatment. Instead, they are cleaned in a special marangoni bath right before further processing. This bath is essentially an HF cleaning bath and rinsing bath, except for one important difference. The wafers are placed vertically in holders and are placed in the bath slowly by a motor. They are also removed from the bath slowly. This allows the marangoni effect to take place, which ensures that any and all remaining water droplets are pulled back into the bath due to the liquid's surface tension.

3.3. PECVD

The photoactive stack of the solar cell is produced using PECVD. PECVD is a deposition technique which deposits layers on a substrate by causing in-flowing gases to become a plasma [40]. In this research, the plasma is created using a radio frequency (RF) or a very high frequency (VHF) generator. Two different PECVD machines are used, because they have access to different precursor gases. Both machines are explained below.

3.3.1. AMIGO

AMIGO is one of the PECVD tools that is used in the EKL lab to deposit different types of layers. In this research, AMIGO is used to deposit the photo-active layers as well as the tunnel recombination junctions (TRJ). These layers include hydrogenated intrinsic nanocrystalline silicon (i-nc-Si:H), n-nc-Si:H, i-a-Si:H, n-a-Si:H, and n-SiO$_X$:H. AMIGO consists of multiple vacuum chambers, each with its own precursor gases. Each chamber is used only for specific types of layers in order to keep the chamber functioning properly. Deposition chamber (DPC) 3 is used to process amorphous silicon, while DPC 4 is used for nanocrystalline silicon. DPC 1 and 2 are used for p-doped and n-doped silicon respectively. DPC 6 is used sparingly to sputter an aluminium zinc oxide (AZO) layer. Sputtering is a different deposition technique which is explained in section 3.4.

3.3.2. Cascade

Cascade is the other PECVD tool which in this research is solely used for GeSn depositions. The end goal is to use GeSn as a low band gap layer in multijunction PEC devices, but first the proper deposition conditions must be found. Cascade functions in a similar fashion as AMIGO. The main relevant differences are that the electrode distance is variable in Cascade, that Cascade has a tetramethyltin (TMT) cannister attached to it to supply it with the tin for depositions and that Cascade is a laminar flow reactor rather than a showerhead reactor like AMIGO.

3.4. Sputtering

Sputtering occurs when a material is bombarded by ions which cause parts of the exposed material to eject from its surface [2]. These ejected particles can then be deposited on a substrate. In this research, sputtering is used to deposit TCO layers via two machines: AMIGO and ZORRO. ZORRO is a cryofox cluster UHV 6 with two deposition chambers. ZORRO is used to deposit ITO and indium tungsten oxide (IWO). ITO is a TCO that is generally positioned at the front and back of the device as shown in figure 3.5. In this research, ITO is also experimented with by positioning it at the interface between separate junctions in an MJ device in order to function as TRJ. IWO and AZO are only experimented with as TRJ.

3.5. Evaporation

The PROVAC pro 500s is a tool that is used to evaporate metals in order to deposit them on substrates. PROVAC utilizes two different evaporation methods. One is resistive heating, which is only used for silver. The other is E-beam evaporation, which focuses an electron-beam on a metal with high enough energy to evaporate it. In this research, PROVAC is used to deposit metals for use as front and back contacts of the solar cell and as intermediate reflective layers (IRLs). The intermediate reflective layer consists of a thin layer of silver in the scale of nanometers in the TRJ at the interface of the bottom and middle junctions. The front contact is made using 500nm aluminium. The back contact is more complex. It uses silver, chromium and aluminium. The silver serves as a mirror to reflect any light that reaches the back contact back into the photo-active part of the solar cell. Chromium serves as an adhesive layer. The aluminium layer is used as proper back contact. Figure 3.5 shows the front side of a finished triple junction stack.
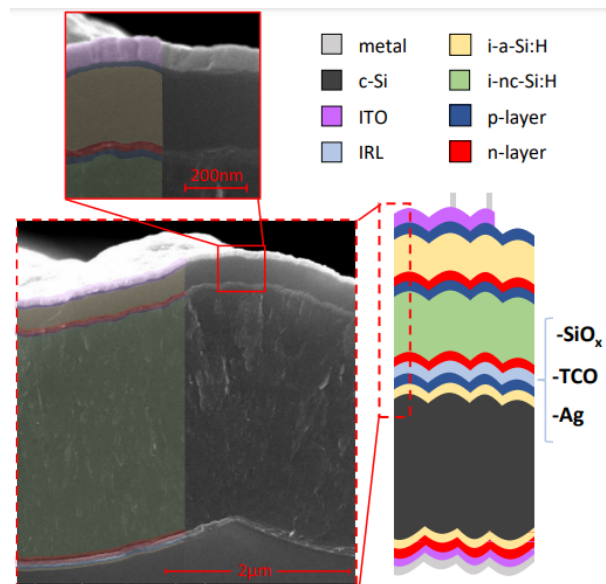
Figure 3.5: Triple junction stack cross-section imaged by an SEM.

4

Measurements

This chapter discusses the ways in which the produced solar cells and glass films are measured. The chapter goes into the optical and electrical characterization of both types of samples, as well as their elemental composition and layer thicknesses. Sections 4.1 JV Curve, 4.2 External Quantum Efficiency, 4.3 Reflectance, 4.4 Cross-section, and 4.5 Spectroscopic Ellipsometry are dedicated to MJ cell measurement. Sections 4.5 Spectroscopic Ellipsometry, 4.6 Fourier Transform Infrared Spectroscopy, 4.7 Energy Dispersive X-ray Spectroscopy, and 4.8 Electrical Conductivity are dedicated to GeSn sample measurement. For the GeSn samples, silicon wafers were used for all measurements except for the electrical conductivity measurements, for which Corning glass films with aluminium contacts were used.

4.1. JV Curve

One important characteristic of a solar cell is its current-voltage (JV) curve. Figure 2.7a shows an example of a JV curve. JV measurements are performed using a WACOM Solar Simulator. The WACOM Solar Simulator produces light with a spectral irradiance reasonably similar to that of the sun by using halogen and xenon lamps. It does so at standard test conditions (STC: AM1.5, $1000 W/m^2$, 25 °C). The ratio of the actual path length of sunlight to the minimal path length is called the optical air mass (AM).

$$AM = \frac{1}{cos\theta} \tag{4.1}$$

Where θ is the angle of incidence of the sunlight. The AM1.5 spectrum therefore refers to the solar spectrum when it hits earth at an angle of 48.2 °.

Before a cell is measured using WACOM, it is first annealed in an oven to improve the contact quality of the metal contacts. A few annealing conditions were tested in this thesis. The best results were achieved by annealing the cells for 10 minutes in an oven at 180 °C.

WACOM enables the measurement of a cell's current as a function of voltage. The results of this measurement are then used to determine the solar cell parameters J_{sc}, V_{oc}, R_s, R_{sh}, FF, I_{mpp}, V_{mpp}, and efficiency. The J_{sc} measurement is used as a first-pass approximation, as it is not very accurate. This is due to its dependence on the illuminated area, which in practice is difficult to keep constant. The metal front contact is difficult to align properly on the front side TCO which causes variations in the illuminated area. Therefore, external quantum efficiency results are used to determine the overall J_{sc}, as well as the J_{sc} per junction.

4.2. External Quantum Efficiency

External Quantum Efficiency (EQE) is defined as the ratio of the amount of collected charge carriers to the amount of incident photons [39]. An in-house set-up is used to measure EQE. A xenon light source and a variable monochromator are used to provide monochromatic light ranging from 300nm to 1200nm. This light passes through a chopper at 123Hz in order to filter out background light. Before measuring a cell, the setup is calibrated using a silicon diode.

In order to measure the EQE of a single junction in a multijunction device, all other junctions must be saturated with light. That way, every electron-hole pair generated in the junction of interest contributes to the J_{sc} of the device without being limited by the other junctions. Saturation is achieved using bias lights. The EQE setup has eight monochromatic LEDs ranging from 365nm to 935nm to provide these bias lights. It is important to saturate the other junction while minimizing the amount of bias light that is absorbed by the junction of interest. To this end, bias lights with energies that approach the band gap energy of the junction of interest are switched off.

4.3. Reflectance

Reflectance measurements are performed using a PerkinElmer LAMBDA 1050+ Spectrophotometer, which measures the wavelength dependent reflection of a cell. Like for the EQE measurement setup, a calibration measurement is necessary. For each silicon wafer the same cell is measured as is measured by EQE. This is done to ensure a complete measurement of a single cell is made, which allows for a direct comparison of the EQE and reflectance.

4.4. Cross-section

A scanning electron microscope (SEM) is used to make images of the cross-section of some cells. These images are used to determine the thickness of each deposited layer in the cell. An FEI Nova NanoSEM 450 is used for cross-section imaging. It uses a focused low energy electron-beam to visualize a cell's surface. See figure 3.5 as an example.

4.5. Spectroscopic Ellipsometry

Spectroscopic ellipsometry (SE) is used to, among other things, accurately measure the thickness of thin films on flat substrates. In this research, a J.A. Woollam M-2000 Ellipsometer is used for SE measurements. In this thesis, SE is used to determine the thickness of various TCO's at specific deposition times, as well as several relevant properties mentioned below for GeSn films.

The ellipsometer is used to measure the polarization by finding the amplitude ratio and the phase difference of the p- and s-components of the reflected light. The angle between the light source and the normal is varied between 55-70 degrees for glass substrates and between 65-75 degrees for silicon substrates in steps of 5 degrees. The wavelength of the light source is varied between 190nm–1700nm [34].

Using CompleteEase software, a Cody-Lorentz model is fitted to the measured data to extract material properties. Among the properties are optical band gap energy (E_{04}), film thickness, refractive index (at 600nm) and absorption coefficient (per wavelength). A fit with a mean square error (MSE) under ten is considered acceptably accurate.

4.6. Fourier Transform Infrared Spectroscopy

Fourier transform infrared (FTIR) spectroscopy is used to obtain an infrared absorption spectrum from a given sample which can then be used to identify which types of chemical bonds are present in the sample. In this research, a Thermo Fisher Nicolet 5700 spectrometer is used which emits infrared light
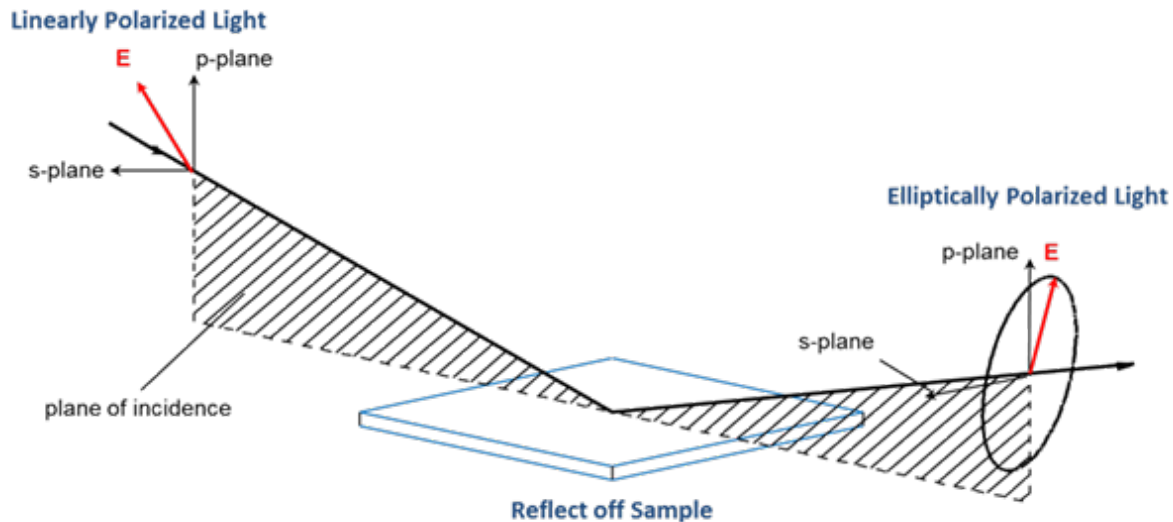
Figure 4.1: A schematic representation of how spectroscopic ellipsometry works [44]. The linearly polarized light becomes elliptically polarized by reflecting off of the sample. The angle of polarization contains information about the sample.

with wavenumbers between 400-4000 cm^{-1}. Wavenumber refers to the amount of periods of a wave occur in a cm and is the inverse of wavelength. The emitted infrared light gets absorbed by a chemical bond when the frequency of the light matches the frequency of a vibrational mode of the bond. A chemical bond has a few vibrational modes: wagging, symmetric stretching, asymmetric stretching, twisting, scissoring and rocking [25]. As it is known which chemical bonds correspond to which wavenumbers, it is possible to identify which bonds are present in the sample.

4.7. Energy Dispersive X-ray Spectroscopy

Energy dispersive x-ray spectroscopy (EDX) is a technique that is used to determine the elemental composition of a sample using an SEM. Electrons are shot at a sample, after which a detector measures the energy of the x-rays that are generated through the interaction of the electrons with the sample. The measured energy spectrum is then used to determine which elements are present in the sample and in which amounts. In this research, an FEI Nova NanoSEM 450 is used for EDX spectroscopy.

4.8. Electrical Conductivity

The electrical conductivity of the GeSn films is measured both with light exposure and without. These measurements are referred to as photoconductivity and dark conductivity respectively.

Photoconductivity is measured using the same WACOM Solar Simulator that is also used for JV measurements, described in section 4.1. Standard test conditions are applied for photoconductivity measurements as well. One important difference is that the voltage is kept constant at 10V. Photoconductivity is calculated using equation 4.2.

$$\sigma_{photo} = \frac{I}{Vbd} \tag{4.2}$$

Where σ_{photo} is the photoconductivity, I is the current at voltage V, b is the ratio of contact length (long side) to the distance between the two aluminium contacts (b=40) and d is the thickness of the deposited layer.

Dark conductivity measurements are done using a Keithley 6517B electrometer. To prevent any photons from reaching the film, a black hood is placed over the entire set-up, the light in the room is turned off and the door to the room is closed. Two probes are attached to the film, a voltage of 10V is applied, the current is measured and the resistance is determined. The same electrometer is used
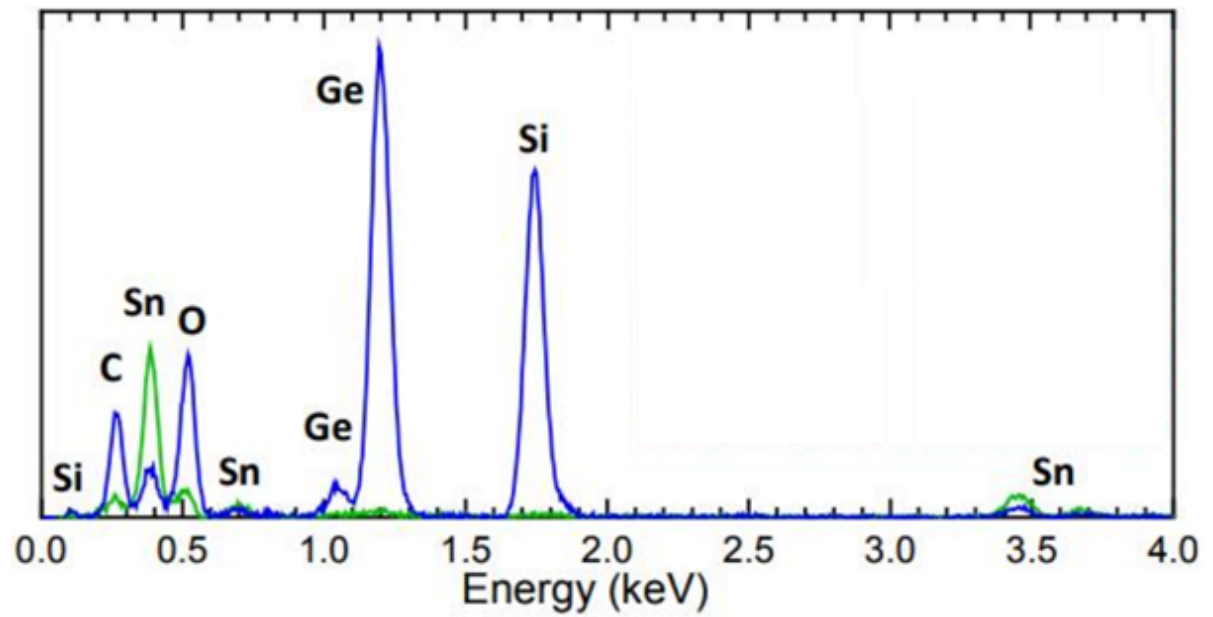
Figure 4.2: An EDX result of a silicon wafer with an a-GeSn:H layer [34]. The green line is the EDX spectrum of a tin cluster on a processed wafer whereas the blue line is the spectrum of the background surface of the same wafer.

to measure the activation energy of each film. This is done by measuring the current at temperatures between 60-130 °C in steps of 5 °C.

$$\sigma_{dark}(T) = \sigma_0 e^{-\frac{E_{act}}{k_B T}}$$

(4.3)

Where $\sigma_{dark}(T)$ is the temperature dependent dark conductivity, E_{act} is the activation energy, k_B is the Boltzmann constant, and T is the temperature in K. Equation 4.3 shows how dark conductivity relates to activation energy and temperature.

5

Results of the Multijunction Series

The focus of this chapter is the quantitative analysis of the redistribution of current density from the bottom junction to the middle junction in c-Si/nc-Si/a-Si triple junction solar cells. In the works which this thesis builds on, the middle junction was generally current limiting [12] [43] [28].

A few approaches are taken to increase the current density in the nc-Si middle junction. Section 5.1 discusses the results of varying the middle or top absorber thicknesses. Sections 5.2-5.4 show the results of introducing IRLs between the n-layer of the middle junction and the p-layer of the bottom junction. Several different materials are tried as IRLs. First, SiO_x in section 5.2, followed by silver (Ag) in section 5.3 and thirdly various TCOs in section 5.4. Finally, the findings of the previous sections are combined to produce and showcase the best performing device of this thesis in section 5.5.

The concepts are first tested in c-Si/nc-Si tandem cells before also being tested in c-Si/nc-Si/a-Si 3J cells. The reason for this order is that tandem cells are easier to fabricate and characterize. On each sample, 22-24 individual $16mm^2$ cells are processed. For JV measurements, all cells are measured and the presented results are the average of the five best cells. For EQE measurements, a few cells (between 2-5 depending on the series) with the best JV responses are measured and the results are presented individually.

5.1. Varying Absorber Layer Thickness

Changing the absorber layer thickness is the simplest way to influence the current density in a junction of an MJ cell. A thicker absorber means there is a higher chance of a photon being absorbed, ultimately resulting in a higher J_{sc} in that junction. However, increased thickness also leads to a higher probability of electron-hole pair recombination which results in a decrease in V_{oc} and FF.

The first absorber layer thickness that is varied is the nc-Si absorber. Increasing nc-Si thickness is a straightforward way to attempt to increase the J_{sc} of this cell. In c-Si/nc-Si tandem cells, the nc-Si absorber is the top cell. In c-Si/nc-Si/a-Si 3J cells, the nc-Si absorber is the middle cell as shown in figure 5.1.

Figure 5.2 shows the V_{oc}, J_{sc} and FF results of varying the nc-Si top absorber thickness between 2.2μm and 4.5μm in c-Si/nc-Si tandem cells. Increasing the nc-Si thickness results in a higher J_{sc} in the top absorber and a lower J_{sc} in the bottom absorber. This indicates that the increase in nc-Si thickness redistributes J_{sc} from the bottom to the top absorber. The current shift is most clearly visible between 2.2μm and 2.7μm, where the top absorber J_{sc} increases from 16 mA/cm^2 to around 18.5 mA/cm^2. Increasing the thickness further leads to diminishing J_{sc} gains. The bottom absorber J_{sc} continues to drop as nc-Si thickness increases. These tandem cell results suggests that the optimal nc-Si thickness is around 2.5μm, because the junctions are current matched around this thickness. However, when analyzing the results of the 3J nc-Si thickness series it will become clear that this is not the case. Adding
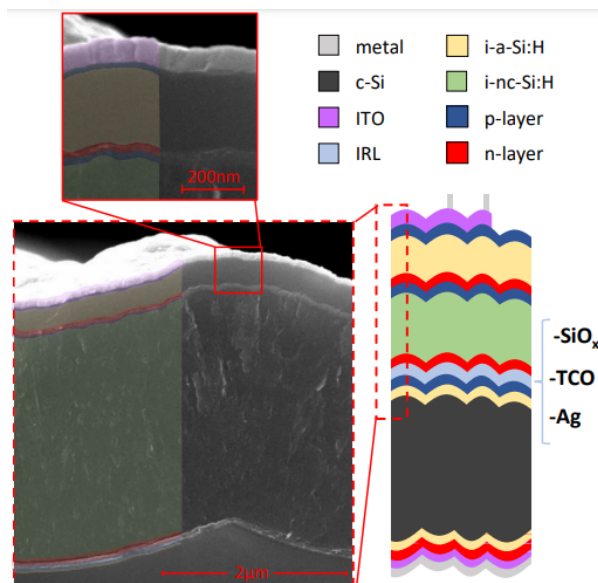
Figure 5.1: Triple junction stack cross-section imaged by an SEM.

a third junction on top of the nc-Si layer has further effects on the J_{sc} of the nc-Si (middle) junction.

The V_{oc} in Figure 5.2 shows a clear decreasing trend with increasing nc-Si thickness. This trend can be explained by an increase in electron-hole pair recombination which occurs in thicker layers. The FF does not indicate such a trend, but instead appears to be decreasing for increasing nc-Si thicknesses. A possible explanation for this is the series resistance of the samples, which show the inverse trend to the FF measurements. The lower the series resistance, the lower impedance there is to the external circuit. This could result in a higher FF and more efficient device.

Figure 5.3 shows the EQE response of the top and bottom cells of the c-Si/nc-Si cells. For the top cell, the biggest difference is seen between 2.2µm and 2.7µm. The top cell EQE of the 2.7µm sample is 0.1 higher than that of the 2.2µm sample for the vast majority of wavelengths between 600nm and 800nm. Increasing the thickness further does not seem to increase the EQE further. The EQE results for the bottom cell behave differently. Increasing the nc-Si thickness decreases the bottom cell EQE response between 2.2-4.4 µm for wavelengths between 600-800 nm. This makes sense, given that the current density of the bottom cell decreases with increasing nc-Si thickness as well.

The results of varying the nc-Si absorber junction thickness in c-Si/nc-Si tandem cells show that increasing nc-Si thickness increases the J_{sc} of the nc-Si top junction at the cost of c-Si bottom junction J_{sc}. This is reflected in the EQE curves, which show that the top cell EQE increases with increasing nc-Si thickness whereas the bottom cell EQE decreases. The V_{oc} and FF of the device decrease with increasing nc-Si thickness excepting the thickest FF measurement, as shown in figure 5.2. All in all, these tandem cell results show that varying the nc-Si top absorber thickness is an effective way to increase the current density in the top junction of a c-Si/nc-Si tandem cell. The reduction in V_{oc} and FF with increasing nc-Si thickness, combined with diminishing returns in top cell J_{sc} suggest that there is an upper limit above which increasing the nc-Si thickness is counterproductive. Next, the effects of varying nc-Si absorber thickness are investigated in c-Si/nc-Si/a-Si 3J cells.

Figure 5.4 shows the results of the 3J series with varying nc-Si middle absorber thickness. Increasing nc-Si absorber thickness leads to higher electron-hole pair recombination resulting in a lower V_{oc}, which is reflected in figure 5.4. FF shows a similar decreasing trend for increasing nc-Si thickness. The J_{sc} curve of Figure 5.4 is very interesting. It shows that the J_{sc} of the middle junction increases with increasing nc-Si thickness, whereas the J_{sc} of the top and bottom junctions decrease. Since the junction with the lowest current is current limiting for the entire device, an nc-Si thickness between 3
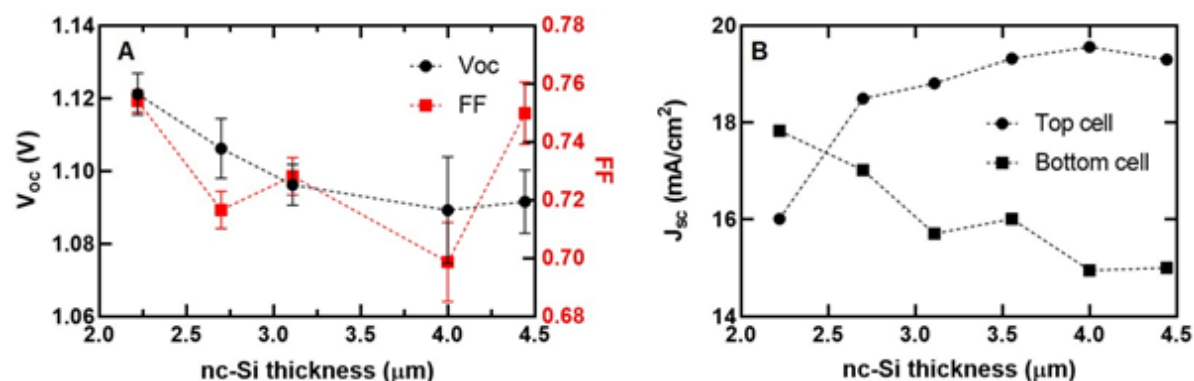
Figure 5.2: These are the electrical results of the tandem c-Si/nc-Si thickness series. The c-Si substrate is kept the same while the nc-Si top absorber thickness is varied between 2 and 4.5 micrometers. The V_{oc} (left) shows a trend, decreasing with increasing nc-Si thickness. The FF (left) shows a similar trend, except for the thickest nc-Si sample. The J_{sc} (right) is shown for both the bottom c-Si cell and the top nc-Si cell. It is clear that increasing nc-Si thickness increases top cell J_{sc} at the cost of bottom cell J_{sc}. The sample with a 3.6μm nc-Si thickness was produced as part of a different series. The V_{oc} and FF of this series deviates from this series and this sample's V_{oc} and FF are therefore left out of this graph. [27]

and 4 micrometers is ideal. This is where the J_{sc} of the top and middle junctions are almost identical. As can clearly be seen, the J_{sc} of the bottom junction is a lot higher than that of the top and middle junctions. Referencing back to Figure 5.2, it can be observed that the addition of an a-Si top junction vastly reduces the J_{sc} of the nc-Si junction, which is now the middle junction, because the a-Si top absorber absorbs high-energy photons which would otherwise have been absorbed in the nc-Si absorber. This is the reason why the relatively large J_{sc} decrease in the bottom c-Si cell is of no consequence and why the small J_{sc} increase in the nc-Si junction is vital.

The total utilisation at an nc-Si thickness of 3.6 μm is 32.0 mA/cm^2. This is 3.5 mA/cm^2 lower than the total utilisation of the tandem cell with a nc-Si top junction of 2.7 μm (35.5 mA/cm^2), suggesting that introducing an a-Si top junction reduces total utilisation. This could be explained by a few phenomena: more parasitic absorption, a higher reflectance, more recombination. To investigate this further, the reflectance graphs of the tandem and 3J cells are compared.

Figure 5.5 shows the reflectance spectrum of a tandem and 3J cell. The tandem cell has the lowest reflectance value around 650nm, where it absorbs nearly 100% of the incoming light. It starts reflecting more light as the wavelength increases, up to 40% at 1200nm, at which point silicon's band gap energy is higher than the photon energy. The tandem cell also has a peak at 400nm. The 3J sample has a reflectance peak at around 700nm as well as between 1000-1100nm. The lower J_{sc} in the 3J cells is to a large degree the result of the difference in the reflectance curves. The tandem cell reflects nearly nothing between 600-800nm, whereas the 3J cell has a very significant reflectance peak around 700nm. This is a region where the AM1.5 spectrum has a very high irradiance, so this reflectance peak could in part explain the difference in J_{sc} between the 2J and 3J cells.

Overall, varying the nc-Si middle absorber thickness is an effective way to adjust the current densities in the bottom and middle junctions. The results in this section indicate that, for a c-Si/nc-Si/a-Si triple junction, nc-Si middle absorber thicknesses between 3-5μm have the potential to improve current matching. Below 3μm, the current in the middle junction is very low compared to the other junctions. Above 5μm, V_{oc} and FF losses outweigh gains in current density.

5.2. Silicon Oxide Thickness

Previous research has shown that silicon oxide (n-nc-SiO$_x$, from this point referred to as SiO$_x$) is an effective n-layer material for TRJs in thin-film devices [11]. It can simultaneously serve as an IRL [7], because the refractive index of SiO$_x$ is around 2 [6], a lot lower than the 3.9 of the surrounding silicon layers [14]. This causes light to be reflected at the interface between SiO$_x$ and the other material. In

nc-Si tandem bottom and top cells EQE
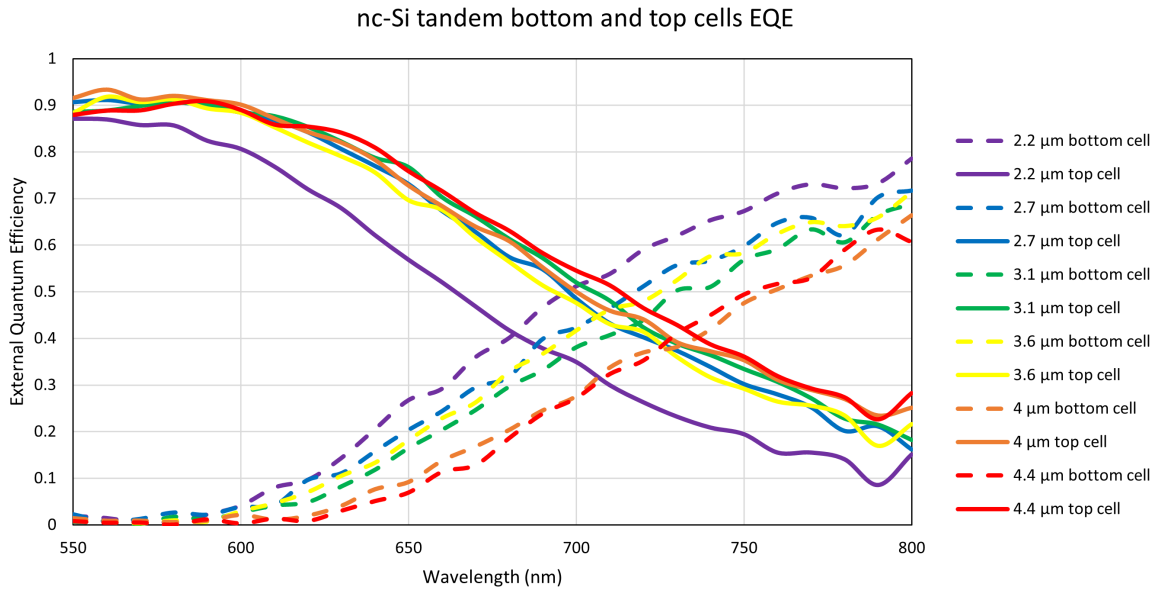
Figure 5.3: EQE results of the c-Si/nc-Si tandem series with varying nc-Si thicknesses in the wavelength region where both the bottom and top cell show significant absorption. For shorter wavelengths, the top cell absorbs the vast majority of incoming light. For longer wavelengths, the bottom cell does so.
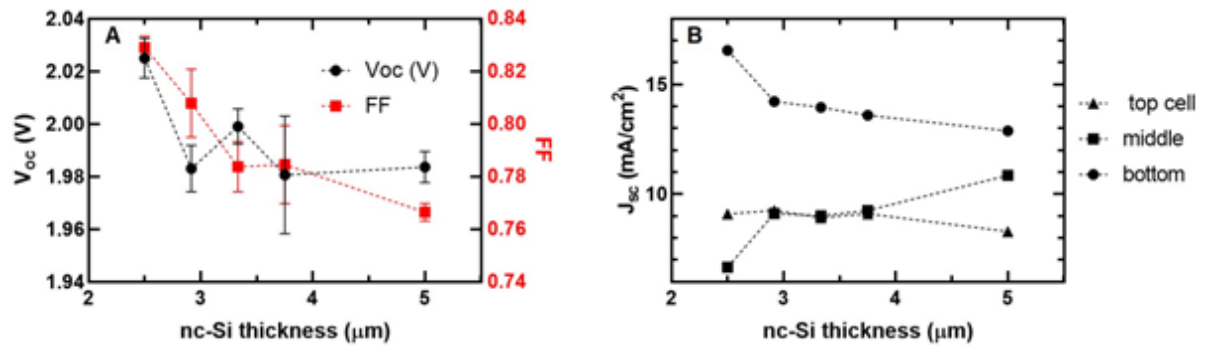
Figure 5.4: The results of the c-Si/nc-Si/a-Si triple junction series where the nc-Si thickness is varied. V_{oc} (left) is shown in black. FF (left) is shown in red. The J_{sc} (right) of each cell is shown. [27]

this case, that other material is nc-Si, as the SiO_x is placed in the TRJ between the middle and bottom junctions. The nc-Si/SiO_x interface reflects some light back into the middle junction which aids in achieving current matching between the cells. Both of these functions of SiO_x depend on the thickness of the layer, so that is what this series looks at. The thickness of SiO_x is varied between 10-60nm in c-Si/nc-Si tandem cells and the results are shown below. Afterwards, SiO_x thickness is varied between 20-80nm in c-Si/nc-Si/a-Si 3J cells.

Figure 5.6 (left) shows that the V_{oc} of the tandem cells decreases with increasing SiO_x thickness. The thinnest sample of 10nm is an outlier with a much higher V_{oc}. The FF increases significantly between 10-30nm, after which it levels off. FF increases when junctions in a 2-terminal MJ device are not current matched. Current mismatch is part of the reason for the observed FF increase with increasing SiO_x thickness, as can be observed in figure 5.6 (right). The current mismatch increases with increasing SiO_x thickness, resulting in a high FF. It is interesting to note that the V_{oc} and FF show opposite trends.

Figure 5.6 (right) shows that increasing the SiO_x thickness increases the J_{sc} of the top cell at the cost of bottom cell J_{sc}. The J_{sc} of the top cell is highest for an SiO_x thickness of 50nm at 22 mA/cm^2, about 3 mA/cm^2 higher than at a SiO_x thickness of 20nm. The 10nm sample is once again an outlier.
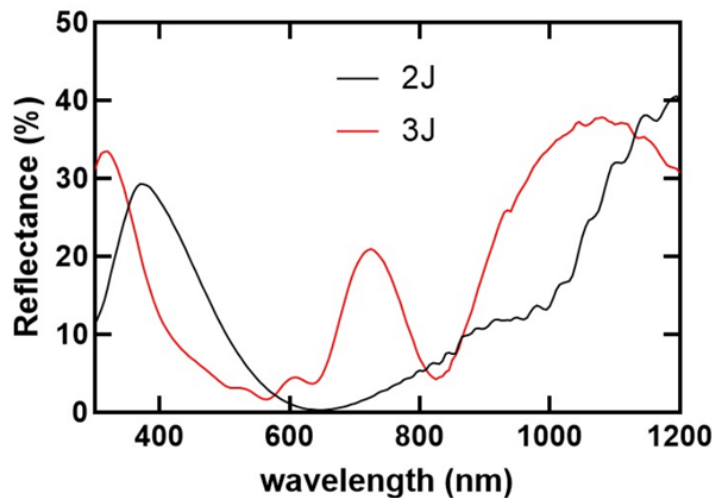
Figure 5.5: The reflectance results for each wavelength for both a tandem and a triple junction cell. The same cell of each sample that was used to measure the EQE is used for The tandem reflectance is shown in black and the triple junction reflectance in red. The nc-Si thickness for the tandem cell sample is around 3.6µm. For the 3J cell it is around 3.75µm. [27]
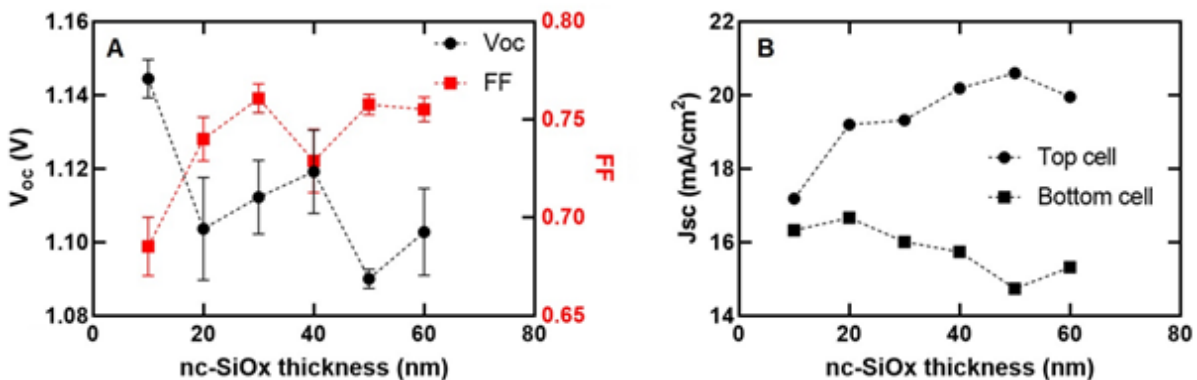
Figure 5.6: The results of the SiO_x thickness series in c-Si/nc-Si tandem cells. The graph on the left shows the V_{oc} and FF. The graph on the right shows the J_{sc} of the top and bottom cells. [27]

The total utilisation of the device fluctuates, without a clear trend towards thin or thick being superior, between 35.3-35.9 mA/cm^2 for a SiO_x thickness between 20-60nm. Therefore, it is safe to say that the SiO_x IRL merely affects the current distribution within the device and does not itself cause a significant reduction in total J_{sc}. These total current values are in the same range as those of the nc-Si thickness series.

Figure 5.7 shows the EQE spectrum of the SiO_x thickness series in the wavelength range where both the top and bottom junctions show significant absorption. Increasing the SiO_x thickness increases the EQE of the top cell. This increase is most significant between 10nm and 20nm and levels off around 40-60nm. The EQE of the bottom cell is highest for the thinnest SiO_x layer and decreases as it gets thicker. The EQE once again levels off as the SiO_x layer gets thicker, with the exception of the device with a 50nm SiO_x layer whose EQE is significantly lower than the other cells.

The tandem cell results for using SiO_x as n-type material and IRL in the TRJ show that it is effective at redistributing current density from the bottom to the middle junction. It also shows that the redistribution scales with SiO_x thickness. No current density is lost in the SiO_x layer itself. The V_{oc} decreases slightly with increasing SiO_x thickness, whereas the FF shows an increasing trend with the exception of the cell with a 40nm SiO_x layer. From these results it is not clear what might happen if the SiO_x layer were to be even thicker, so a cell with 80nm is produced in the 3J series.

c-Si/nc-Si tandem with SiOx IRL, bottom and top EQE
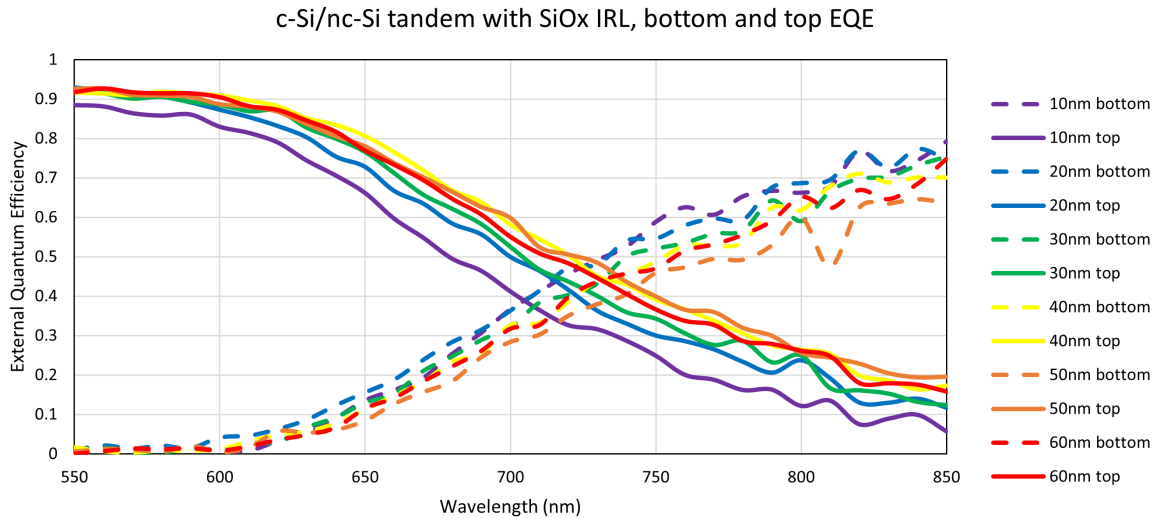
Figure 5.7: The EQE of the top cell (solid lines) and the bottom cell (dotted lines) for the SiO_x thickness series.
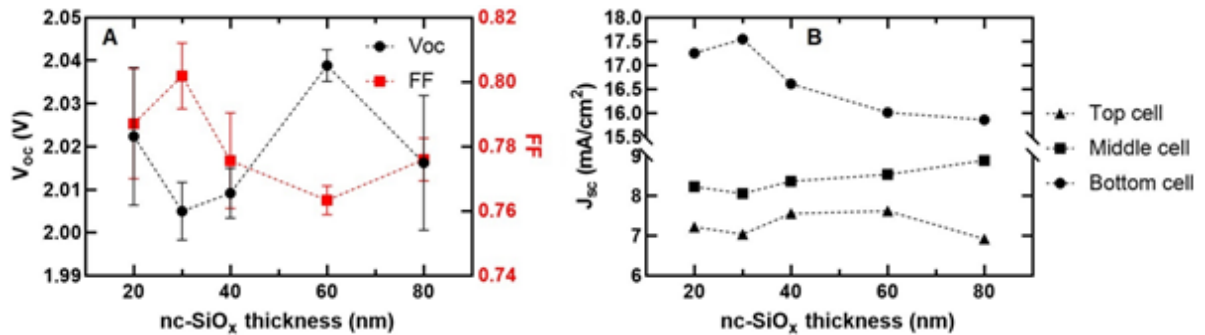
Figure 5.8: The results of the SiO_x thickness series in c-Si/nc-Si/a-Si 3J cells. The graph on the left shows the V_{oc} and FF. The graph on the right shows the J_{sc} of the top, middle and bottom cells. [27]

The results from the SiO_x tandem series inspired the thickness range for the 3J series. Because the 10nm cell behaved poorly compared to thicker cells for the given reasons, it was not included in the 3J series. Instead, a cell with 80nm SiO_x was included.

Figure 5.8 shows the V_{oc}, FF and J_{sc} for the 3J series. The V_{oc} and FF once again show opposing trends, one increasing when the other decreases, except for the sample of 80nm. The highest FF is also once again observed at at SiO_x thickness of 30nm. However, increasing the thickness further decreases the FF in the 3J series as opposed to the increase in FF that occurred in the tandem series. An explanation for this observation is the fact that the increased thickness results in an improved current matching in the 3J series, whereas in the 2J series the current mismatch increased.

The bottom cell J_{sc} drops from 17.6 mA/cm^2 to 15.9 mA/cm^2 between 30-80nm. This drop is accompanied by a middle cell J_{sc} increase from 8.1-8.9 mA/cm^2 and a top cell J_{sc} change from 7.0-6.9 mA/cm^2. In total, 1.7 mA/cm^2 is lost in the bottom cell and 0.7 mA/cm^2 is gained in the middle and top cells. It is interesting to note that the introduction of SiO_x resulted in a smaller device level J_{sc} drop than increasing the nc-Si thickness did. However, in this series the current mismatch between middle and top cells was markedly higher. The top cell was current limiting, having a >1 mA/cm^2 lower J_{sc} than the middle cell throughout the whole series. This could be improved by increasing the a-Si top junction thickness.

Overall, using SiO_x as an IRL in 3J is an effective way to adjust current densities in c-Si/nc-Si/aSi triple junction PV devices. Although the total utilization of the 3J devices with an SiO_x IRL decreased

with increasing SiO_x thickness, the middle junction J_{sc} markedly improved with increasing SiO_x thickness. The bottom junction J_{sc} loss was responsible for most of the total utilization decrease. Considering that the J_{sc} of the bottom junction is significantly higher than those of the middle and top junctions, this loss is acceptable. The electrical properties, V_{oc} and FF, remained at high levels for all SiO_x thicknesses.

5.3. Silver Intermediate Reflective Layer Thickness

Even with SiO_x serving as an IRL, the bottom junction has a far higher J_{sc} than the middle and top junctions. The addition of another IRL may help to redistribute the device J_{sc} more favorably. Silver is tried as an IRL in the next experiments.
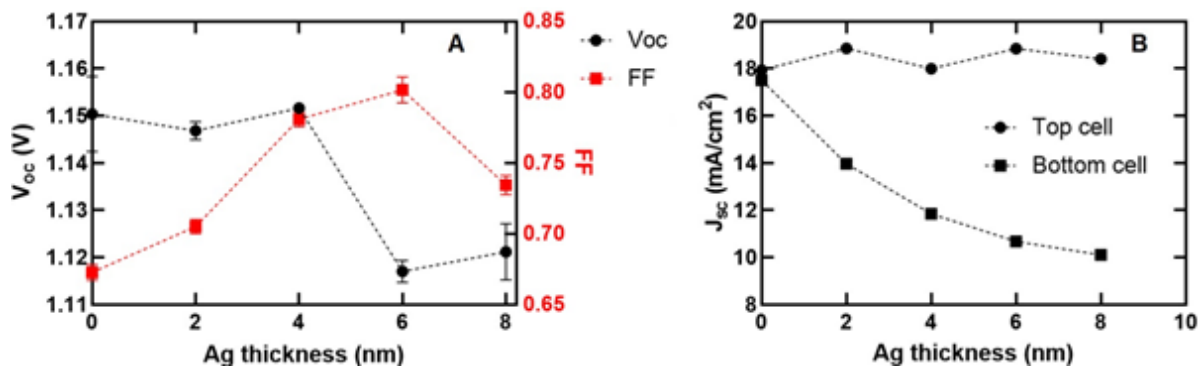
Figure 5.9: The V_{oc}, FF (left) and the J_{sc} (right) of the Ag thickness tandem series. [27]

Figure 5.9 (right) clearly shows that the J_{sc} of the bottom cell decreases as Ag thickness increases. However, there does not seem to be the expected corresponding increase in top cell J_{sc}. This suggests that the silver layer absorbs light rather than reflect it. The added silver layer does however have electrical benefits as can be seen in Figure 5.9 (left). Between 0-4nm the V_{oc} stays constant around 1.15V while the FF increases from 0.67 to 0.78. Further increases to the silver thickness past 4nm result in a decrease in V_{oc} to 1.12V. A possible explanation for this decrease is the recombination of electron-hole pairs in the conductive silver layer, which could also explain part of the reduction in J_{sc} in the bottom junction. The increase in FF may be because of improved electrical performance of the TRJ due to the introduction of silver, or it may be a consequence of the current mismatch between the bottom and top junctions.
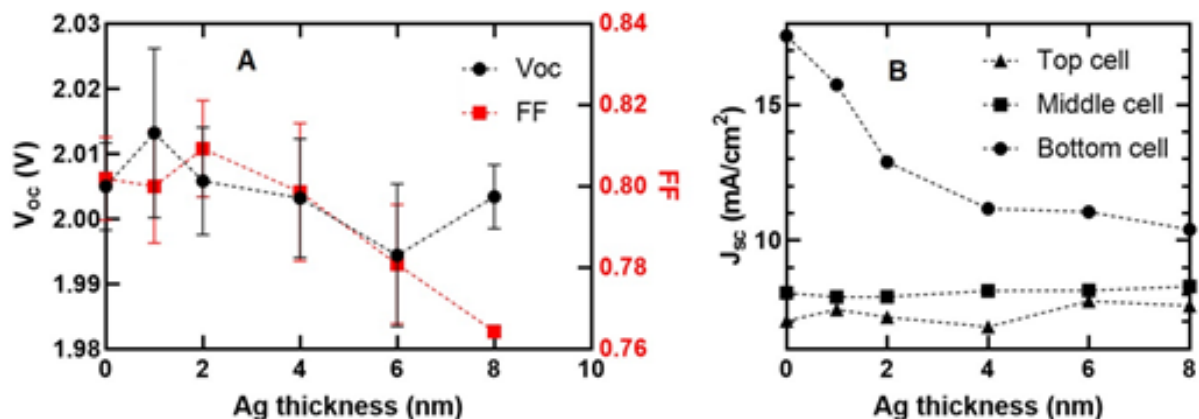
Figure 5.10: The V_{oc}, FF (left) and the J_{sc} (right) of the Ag thickness 3J series. [27]

Next, silver is introduced at the interface between the n-layer of the middle junction and the p-

layer of the bottom junction of 3J cells. Figure 5.10 (left) shows no clear trend in V_{oc}. FF decreases with increasing Ag thickness. This is likely due to improved current matching, as the bottom cell J_{sc} approaches that of the middle and top junctions. The V_{oc} of the 1nm Ag sample is highest of all samples, but also has the largest error margin. The 2nm sample has a peak in FF even though the junctions are more current matched the 0nm and 1nm samples. This observation is similar to the FF results in the tandem cells with Ag. Again, the reason is likely the improved electrical conductivity that is a result of introducing silver into the TRJ [19].
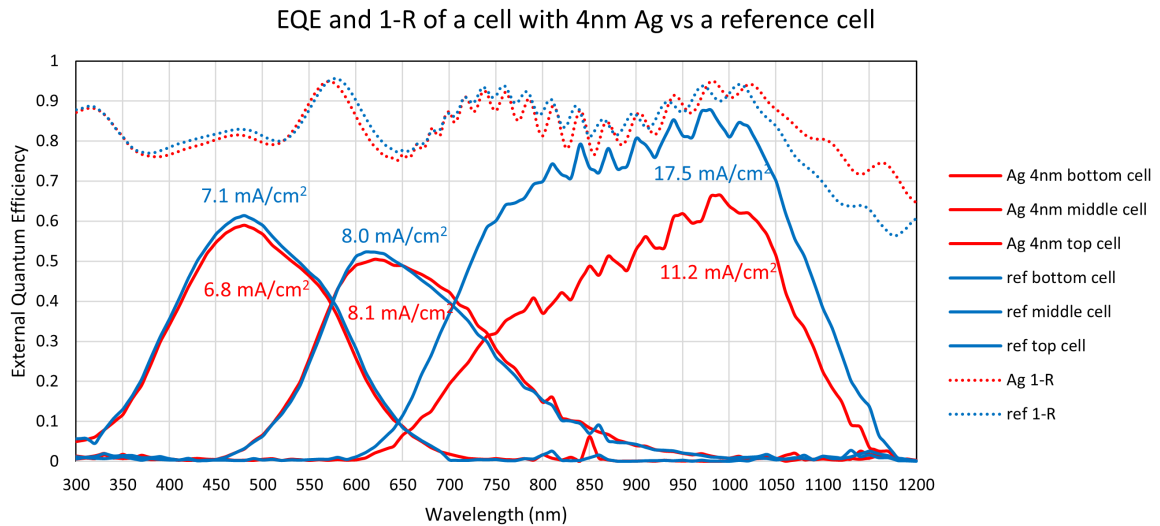
Figure 5.11: EQE and 1-R comparison of a 3J with a 4nm Ag IRL layer and a reference cell without Ag.

It is clear that the 3J cell with 4nm Ag has a significantly lower bottom cell J_{sc} than the reference cell. This is compensated to some extent by the slight increase in the J_{sc} of the middle junction of the Ag cell. Considering that the middle cell is current limiting, this may be a worthwhile trade-off to slightly improve the device J_{sc}.

The fact that only a minute portion of the bottom cell J_{sc} is redistributed to the middle cell in the Ag device suggests that the silver absorbs light rather than reflect it. Otherwise, one should expect the middle and top absorbers to gain a total of 6.3 mA/cm^2.
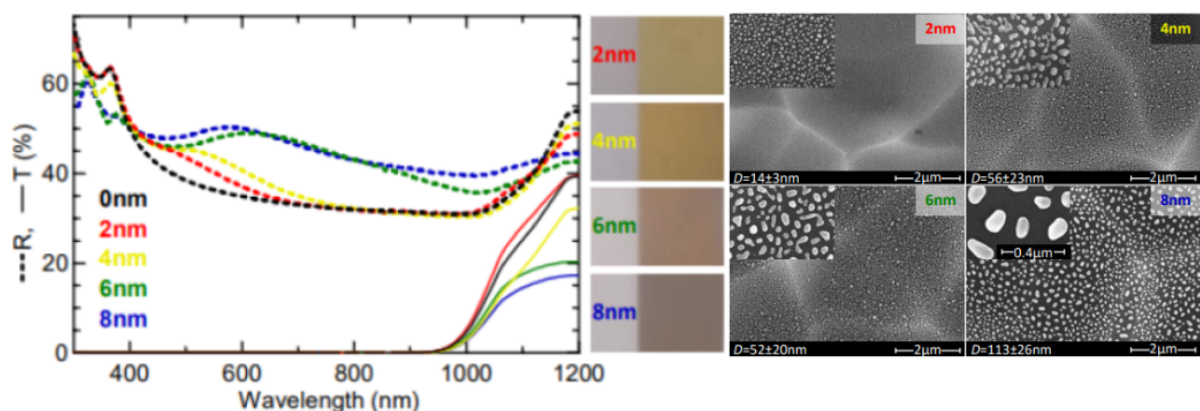
Figure 5.12: Reflectance and transmittance measurements of Ag films on textured wafers. In the middle are pictures of each Ag thickness on the glass films. On the right side are four SEM images of said films. It can be observed that the silver forms clusters. The clusters become larger and further apart with increasing silver thickness. [27]

Figure 5.12 (left) shows that the reflectance of the Ag films increases with increasing Ag thickness

between 400-1100nm. The transmittance between 1000-1200nm decreases with increasing Ag thickness. At this wavelength range, the reflectance does not increase with Ag thickness. This suggests that thicker silver layers absorb more light.

Figure 5.12 (right) shows that the silver formed nanoscale islands rather than a layer. Increasing the thickness of the silver accentuated this effect, creating bigger silver islands that are spaced further apart from each other. Silver grows according to the Volmer-Weber growth model: nanoscale islands form rather than a layer. The formation of islands results in different (reflective) properties of this silver IRL compared to a thicker, smooth layer.

Overall, using silver as an IRL does not seem to be an effective way to adjust current densities in c-Si/nc-Si/a-Si triple junction PV devices. The top junction J_{sc} decrease was accompanied by an ever so slight increase in the middle junction of 0.1 mA/cm^2 and a decrease of 0.3 mA/cm^2 in the top junction using a 4nm Ag IRL. The V_{oc} of the 3J device with a 1nm Ag layer increased slightly. However, the added costs, deposition time and processing complexity do not warrant the inclusion of a silver layer with so few benefits.

5.4. Transparent Conductive Oxides in the Tunnel Recombination Junction

Transparent conductive oxides (TCOs) can serve as IRLs due to their low refractive index compared to neighbouring materials. Furthermore, TCOs are very conductive. Finally, they are transparent to visible light. All of these properties combine to make TCOs perfect for use in TRJs. There is a trade-off to be made between conductivity and transparency, because while conductivity increases with TCO thickness, transparency decreases with thickness. One potential benefit of using TCOs in a TRJ is that the thickness can be tuned so that specific wavelengths are reflected more readily due to interference. This would allow more light in the 500-800nm range to be reflected while more light in the >800nm range would pass through the TCO. This way, the TCO acts as an IRL for some wavelengths while being transparent to other wavelengths.

5.4.1. Indium Tin Oxide

A few different configurations were tried when Indium tin oxide (ITO) was introduced in the TRJ. Figure 5.13 (C) shows the different configurations. ITO, ITO with an n-a-Si buffer layer to protect the ITO layer against damage from later depositions, ITO + aluminium zinc oxide (AZO), and ITO + silver + AZO were tried. These results indicate that using multiple reflective layers in combination with each other (ITO + AZO, ITO + Ag + AZO) is better than just using ITO in terms of V_{oc}*FF product. The V_{oc}*FF product is used as a single measure for the electrical performance of the cells. All cells with a TCO perform worse than the reference sample.

The V_{oc}*FF product of the tandem cell decreases rapidly when introducing ITO. This can be explained by the steep reduction in R_{sh} that also occurs when introducing ITO. The low shunt resistance provides an alternative path for the electricity to travel.

What causes the steep reduction in R_{sh} that goes along with the introduction of ITO into the TRJ? It is a possibility that the conductive ITO electrically connects shunting paths through the nc-Si top junction and the SHJ. Another possibility is that the deposition of ITO damages the SHJ, or that the deposition of nc-Si damages the ITO. Indium tungsten oxide (IWO) is chosen as an alternative TCO to test this damage hypothesis in part. IWO is deposited at room temperature, which reduces the likelihood that it may damage the SHJ below it. The deposition of nc-Si could still damage the IWO though. Considering that the addition of AZO improved the V_{oc}*FF product compared to just using ITO (see figure 5.13 C), it was decided to test whether AZO without ITO had even more beneficial electrical properties.
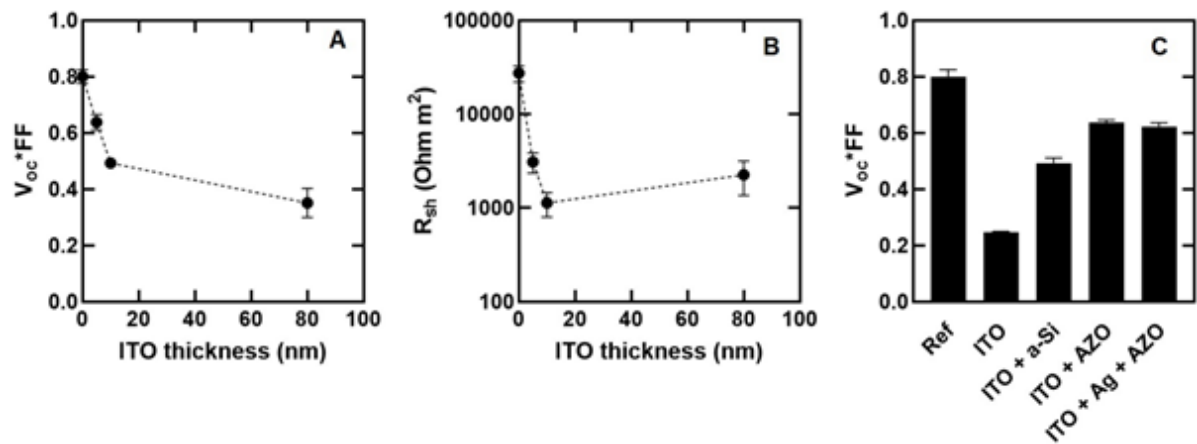
Figure 5.13: The effects of adding ITO to the TRJ of a c-Si/nc-Si tandem cell. The left graph shows the V_{oc} *FF product. The middle graph shows the shunt resistance R_{sh}. The right graph shows the V_{oc} *FF product of varying compositions (ITO, ITO + n-a-Si:H, ITO + AZO, ITO + Ag + AZO) [27].
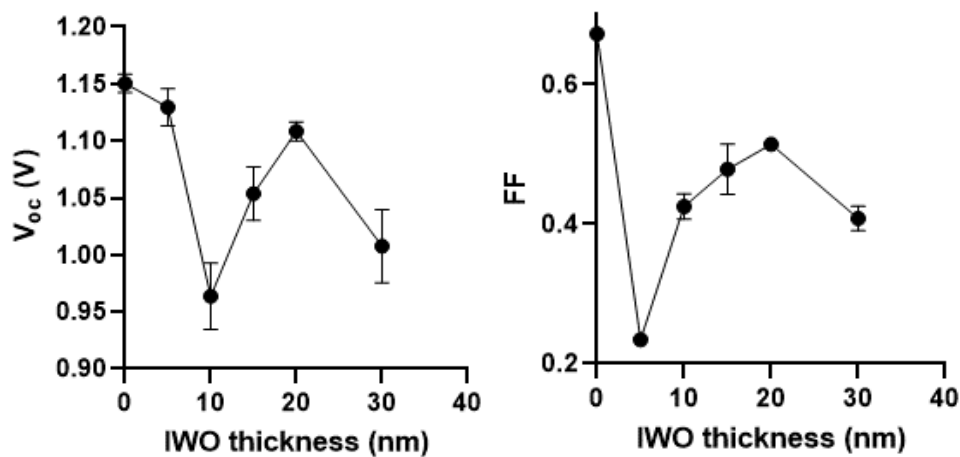
Figure 5.14: V_{oc} and FF for c-Si/nc-Si:H tandem cells with IWO in the TRJ.

5.4.2. Indium Tungsten Oxide

The V_{oc} of the IWO cells shows a decreasing trend with increasing IWO thickness in figure 5.14. The FF of all IWO cells is very low compared to the reference sample. Increasing IWO thickness does not seem to cause a further decrease in FF. The FF outlier at an IWO thickness of 5nm can be explained by the extremely high series resistance of this cell, which is shown in figure 5.15a.

R_{sh} shows a local peak at 15nm IWO thickness in figure 5.15b. The reason for this is unclear. It is also in the same order of magnitude as the ITO cells in figure 5.13 (B). This observation suggests that the low R_{sh} of these cells is not due to damage to the SHJ that would have occurred during the deposition of the ITO.

5.4.3. Aluminium Zinc Oxide

Using AZO as TCO in the TRJ of c-Si/nc-Si:H tandem cells showed more potential than ITO, so it is tested next. Edge shunting (shunting along the edge of the wafer) might be causing the low shunt resistances in the cells with TCOs. To account for this, the AZO cells were scribed with a diamond pen around the edges of the wafer. This cuts through the AZO layer and all junctions on top of it, into the c-Si substrate, electrically isolating the cells from the edge of the wafer.

(a) IWO series resistance

(b) IWO shunt resistance
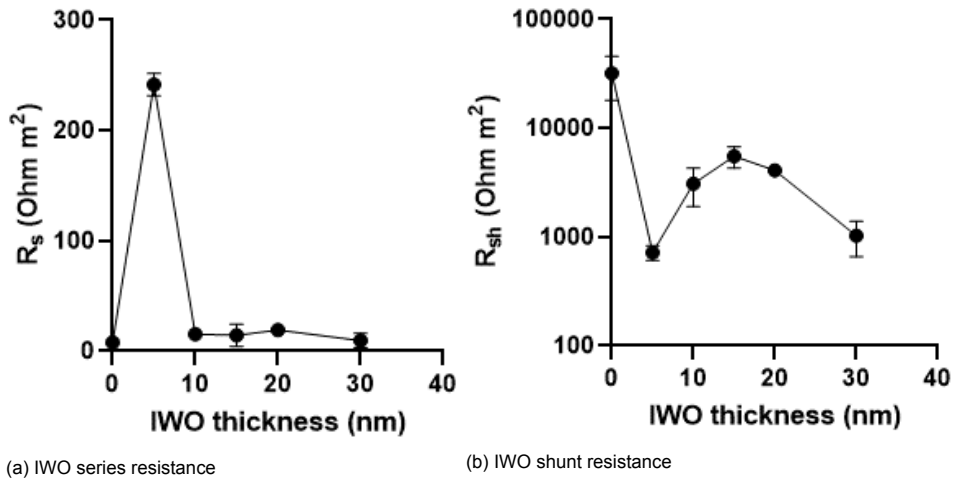
Figure 5.15: Rs and Rsh for c-Si/nc-Si:H cell with IWO in the TRJ.
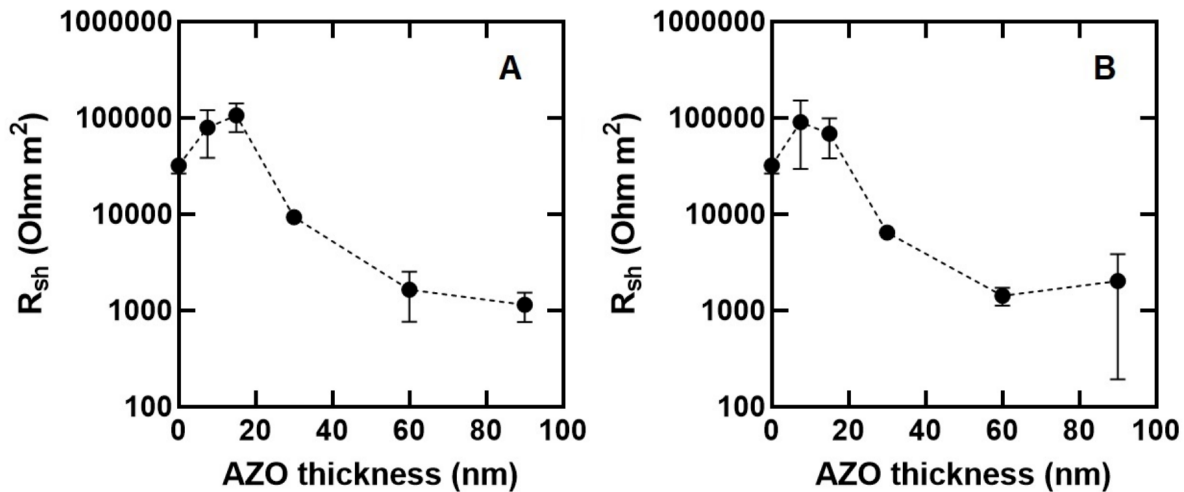
Figure 5.16: Shunt resistance for c-Si/nc-Si:H tandem cell with AZO in the TRJ before scribing (A) and after scribing with a diamond pen to isolate cells from the edge (B) [27].

Figure 5.16 shows that there is little to no difference in R_{sh} before and after scribing the edges of the c-Si/nc-Si:H tandem cell with AZO in the TRJ. This suggests that the decreasing shunt resistance as the AZO gets thicker is due to shunting in the cell(s) rather than edge shunting. In order to test this more thoroughly, some AZO cells were broken off from the rest of the wafer to isolate them completely. This is a difficult process and resulted in some cells losing some cell area, rendering those cells useless for measurements. The few cells that were fit for measurement gave varying results. Only a single cell gave a shunt resistance of more than $10^5 \Omega m^2$. The other fragments showed only slight improvements over the initial shunt resistance measurements. In subsequent experimental runs, a mask was used during the TCO depositions, and every deposition following the TCO deposition, in order to eliminate bulk shunting between cells on the same wafer.

Figure 5.17 shows the shunt and series resistances of triple junction cells with varying AZO TRJ thicknesses deposited through a mask. It is clear that the shunt resistance of these cells is still significantly lower than the comparison cell without AZO. However, the shunt resistance values of the triple junction cells are in the same order of magnitude as triple junction cells without AZO in this thesis. The shunt resistances are also more than an order of magnitude higher than the previously measured ITO and IWO cells. However, considering that one is a 3J while the others are tandem cells, this comparison may not be totally sound.
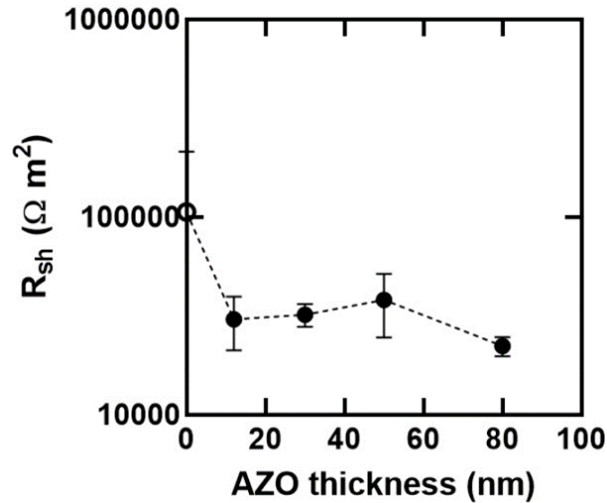
Figure 5.17: The shunt resistance data point without AZO is from another series and is provided as reference. The shunt resistance is relatively low in the cells with AZO. The series resistance drops slightly after an initial increase. [27]
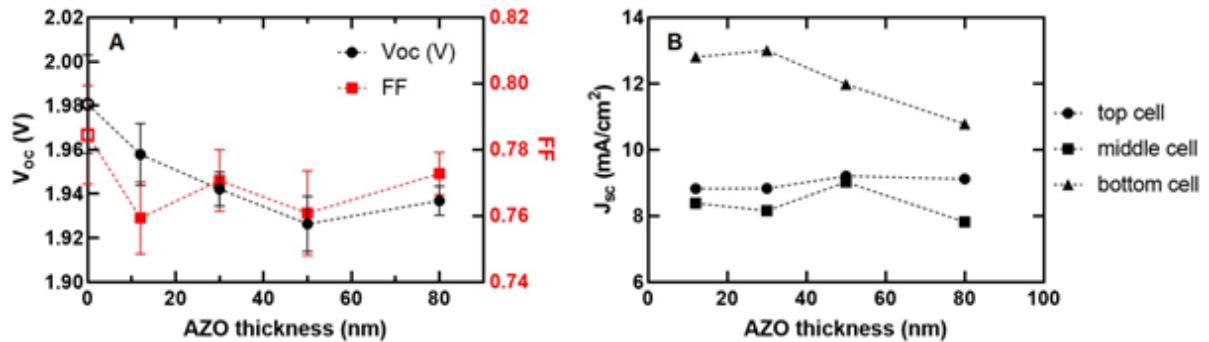
Figure 5.18: The V_{oc} and FF (left) and the J_{sc} (right) of 3J cells with varying AZO thicknesses. [27]

There is a clear decreasing trend in V_{oc} with increasing AZO thickness in figure 5.18. The FF closely follows the V_{oc} trend, except for the 10nm sample, where both V_{oc} and FF have a large error margin. The drop in V_{oc} and FF is not nearly as large as in the original 3J measurements where the AZO TRJ is not deposited using a mask to isolate individual cells. The bottom cell J_{sc} clearly decreases for increasing AZO thickness, but this is not accompanied by an increase in middle or top cell J_{sc}.

The EQE graph shown in figure 5.19 may offer some insights into the reasons for this bottom cell J_{sc} decrease. The 1-R of the device with AZO is 0.10-0.15 higher than the 1-R of the reference device in the 400-550nm range in figure 5.19. This is reflected in the top cell EQE of the device with AZO, which is significantly higher than the top cell EQE of the reference device. Interestingly, the peak EQE of the reference device middle cell is higher than the peak EQE of the middle cell of the device with AZO even though the 1-R of the reference device is 0.1 lower than the 1-R of the device with AZO around this point (600-650nm). This suggests that parasitic absorption and reduced carrier collection, rather than photon absorption, are in part responsible for the low middle junction J_{sc} in the device with AZO. The reference device has a significantly higher 1-R than the device with AZO in the 950-1200nm range. The difference in bottom cell EQE between the device with AZO and the reference device is even larger than that difference in 1-R. This suggests that both parasitic absorption and reduced carrier collection play a role in the low bottom cell EQE of the device with AZO.

The current density of the middle junction with AZO is 0.2 mA/cm^2 lower than the reference junction. The total utilisation of the reference and AZO devices are 32.6 mA/cm^2 and 27.8 mA/cm^2 respectively.
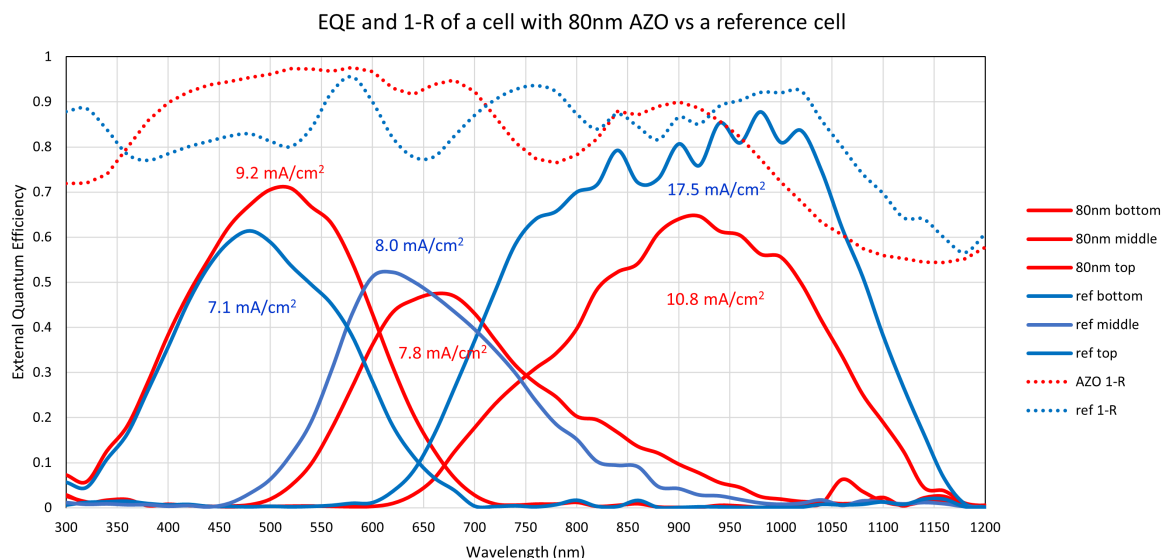
Figure 5.19: The EQE and 1-R results of a reference 3J cell (dark colours) and a cell with 80nm AZO as IRL in the bottom-middle TRJ (light colours).

In order for the AZO TRJ to be beneficial, a way to bring the EQE closer to 1-R must be found. Reducing parasitic absorption and increasing charge carrier collection. Another option is to reduce R, preferably in the 700+nm range, but especially in the 950+nm range. One way to attempt this is to test different surface textures.

Overall, introducing TCOs between the n-layer of the middle junction and the p-layer of the bottom junction in c-Si/nc-Si/a-Si devices results in worse V_{oc} and FF, as well as lower J_{sc} in the middle (current limiting) junction. The shunt resistance of most measured cells with TCOs were significantly lower than the shunt resistances of cells without TCOs. TCOs should therefore not be used as IRLs in these device architectures.

5.5. Combining Effects

Both the nc-Si thickness series and the SiO_x thickness series showed promising results. This section discusses the results of a run which aimed to combine these effects to produce a high performance device. The best performing device was produced using a 400nm a-Si:H absorber, a 4.5µm i-nc-Si:H absorber and a 60nm SiO_x IRL. The device had a V_{oc} of 1.947V, FF of 0.789 and a J_{sc} of 9.51mA/cm^2 (the i-nc-Si absorber is current limiting as shown in figure 5.20), resulting in an overall efficiency of 14.6%.

Figure 5.20 shows the champion cell of this thesis. It can be seen that the total utilisation exceeds 1-R around 850nm. This is due to an emission peak of the xenon lamp used in the setup which proved challenging to remove, even with a calibration measurement done beforehand.

The EQE graph shows that the current density of the top cell is still higher than that of the middle cell. Simply decreasing the a-Si:H absorber thickness would decrease the top cell J_{sc} and increase the middle cell J_{sc}. transfer some current density away from the top cell into the middle cell. The total utilisation of the champion device is 34.2 mA/cm^2, which is roughly 2 mA/cm^2 higher than the other devices in this chapter.
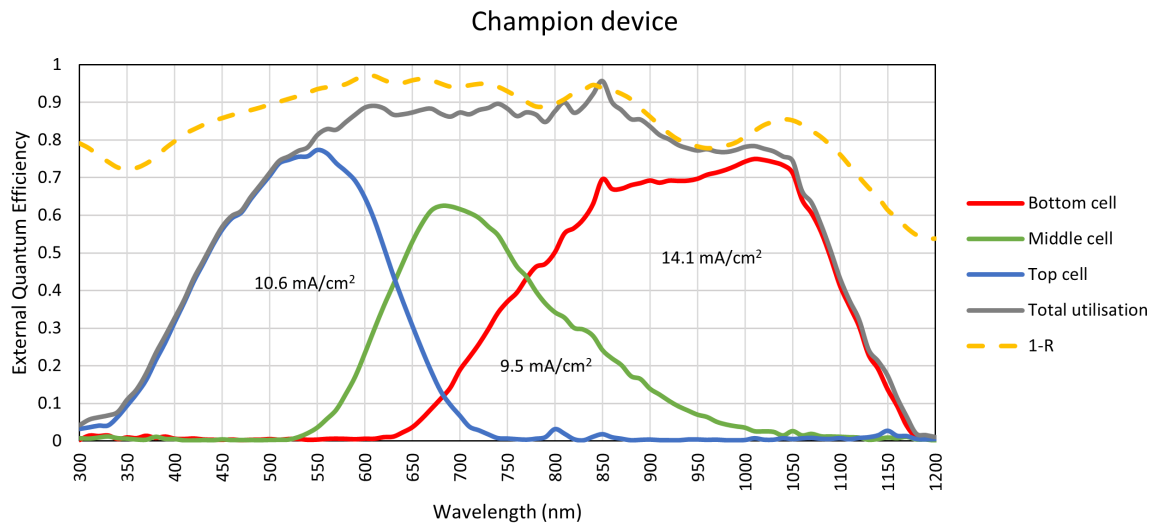
Figure 5.20: The EQE of the bottom, middle and top cells, as well as the total utilisation and 1-R of the best performing cell in this thesis. The total utilisation exceeds 1-R at 850nm due to a measurement error that occurs in the inhouse EQE set-up when the light source is switched.

6

Results of Germanium Tin Series

It is useful for MJ PV devices to be able to use a low bandgap semiconductor material as absorber layer in the bottom junction in order to be able to finely tune the output voltage of the device. Hydrogenated germanium tin (GeSn:H) is investigated as a potential option for this function. GeSn:H can be produced using PECVD, meaning that the production of a complete device that also uses c-Si, nc-Si and/or a-Si absorbers can be performed in a single PECVD machine. This integration makes the production process more efficient.

The goal of the GeSn:H experiments is to produce device quality films for MJ PV devices. To achieve this, the influence of deposition conditions on GeSn film material structure, and by extension its opto-electrical properties, are investigated. In total, the influence of six different deposition condition variables on characteristic material properties was investigated: Tetramethyltin (TMT) flow, germane flow, helium flow, temperature, pressure, and power.

What does it mean for a GeSn:H film to be of device quality? First of all, it must be intrinsic, meaning that the Fermi level is halfway between the valence band edge and the conduction band edge. Another way to say this is that the activation energy is half of the bandgap energy (E_{act} = 0.5E_{04}). An intrinsic GeSn:H film can be used in an n-i-p configuration. The film must have a bandgap below 1.0eV and a high photoresponse to obtain a high current density.

A precursor gas is required to inject tin into the deposition chamber of Cascade. Previous research on Ge:H used GeH_4 as precursor gas [34]. However, tin bonded to four hydrogen atoms, SnH_4, is unstable. Therefore, an alternative precursor gas must be found. There are several options such as $SnCl_4$, tetra-ethyltin [$Sn(C_2H_5)_4$] and tetra-methyltin [$Sn(CH_3)_4$] (TMT) [10]. TMT is chosen as precursor gas, because it is commercially available, consists of only group IV elements and is a relatively simple molecule. TMT is a liquid at room temperature, so it is heated before being injected into the deposition chamber via an atomic layer deposition (ALD) valve.

An ALD valve was used to control the TMT injection rate into the DPC. This valve is capable of opening and closing for precise, short intervals. This enables control over the TMT injection rate.

For all series, the presented results include the refractive index at 600nm ($n_{@600nm}$), optical bandgap energy (E_{04}), photoresponse ($\sigma_{photo}/\sigma_{dark}$), activation energy ($E_{act}$), and dark conductivity (σ_{dark}). Some results also present the growth rate in nm/min.

The author processed the samples and collected measurement data together with Federica Saitta. All data analysis and data visualisation was done by Koos Roodenburg [34]. Nevertheless, the author has attempted to interpret the results within the context of GeSn:H being used as a bottom cell in MJ devices.

Section 6.1 discusses the effects of varying the TMT flow rate on the produced films. Secondly, section 6.2 presents the effects of adding helium to the gas flow mix as a diluting agent. After that,

section 6.3 talks about the effects of varying the temperature. Section 6.4 varies the germane flow and discusses those results. Finally, the results of varying pressure and power are presented in section 6.5.

6.1. TMT Injection

The TMT injection into the reactor is controlled by an ALD valve. Each cycle, the valve has an open time and a close time. The duty cycle (δ) of the ALD valve is defined as the close time divided by the open time. A high δ therefore corresponds to a low TMT injection. In the three close time series (yellow, red and blue), the close times are 5s, 10s, 20s, 30s, and 40s or 50s. In the open time series (purple), the open time is set to 5ms, 6ms, 7ms and 8ms. The deposition conditions of the results shown in figure 6.1 are shown in appendix B.1.
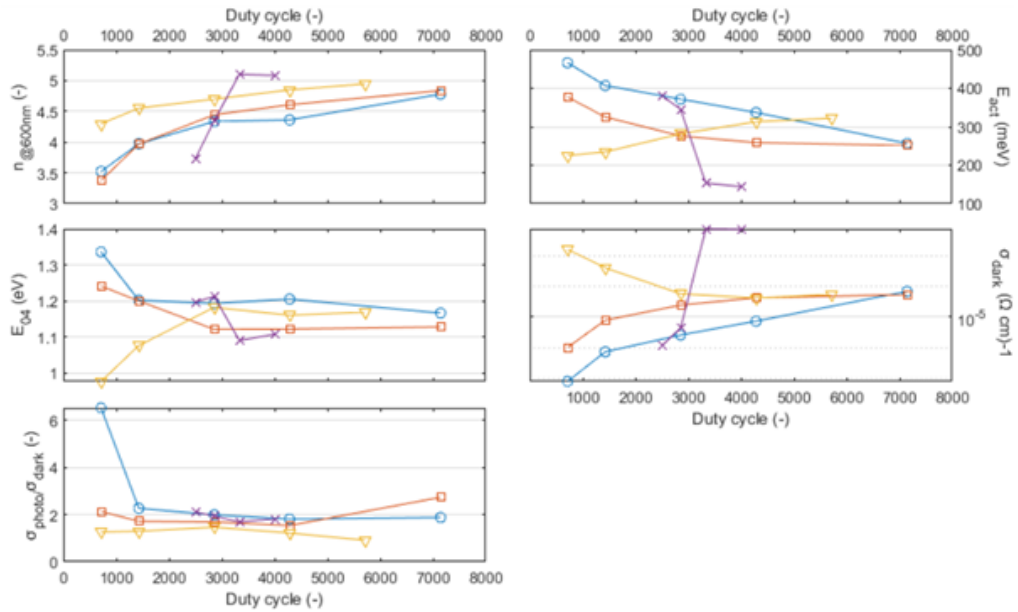
Figure 6.1: Results of varying the duty cycle of four series. The yellow data is the nc-GeSn:H series. The blue, red and purple data are a-GeSn:H series corresponding to the deposition conditions of the same colour series in appendix B.1. The close time is varied in the yellow, red and blue series. The open time is varied in the purple series. [34]

The concentration of carbon in the films increased drastically as a result of TMT injection relative to earlier Ge:H samples [34]. This carbonization has a major impact on the material structure of the GeSn:H films. Namely, the carbon passivates dangling germanium bonds in the film. As a result, the activation energy increases with increased TMT injection for the a-GeSn:H films as shown in figure 6.1. The nc-GeSn:H films show the opposite trend. The reason for this is unclear to the author.

Figure 6.1 shows that the refractive index increases as δ increases for every series. On the surface this makes sense, because tin has a lower refractive index (2.4 at 632.8nm [15]) than germanium (5.5 at 632.8nm [13]) and silicon (3.9 at 632.8nm [14]). However, there may be a different reason for this change in refractive index. Introducing TMT into the deposition chamber not only increases the concentration of tin and carbon on the films, but also the concentration of oxygen, as shown in figure 6.2. Oxygen is not part of the plasma during deposition. A likely explanation for its presence is post-processing oxidation. The presence of oxygen is therefore an indication that the produced GeSn:H films are not chemically stable. Increased concentrations of carbon and oxygen also indicate a higher level of porosity in the films. The decreasing refractive index for increasing TMT injection rates may therefore be a consequence of increased porosity in the film, rather than an inherent difference in the refractive indices of the elements in the film.

The optical bandgap energy converges to a value between 1.1-1.2 eV as δ increases. The dark conductivity (σ_{dark}) scales inversely with E_{act} as shown by equation 4.3. Consequently, the highest
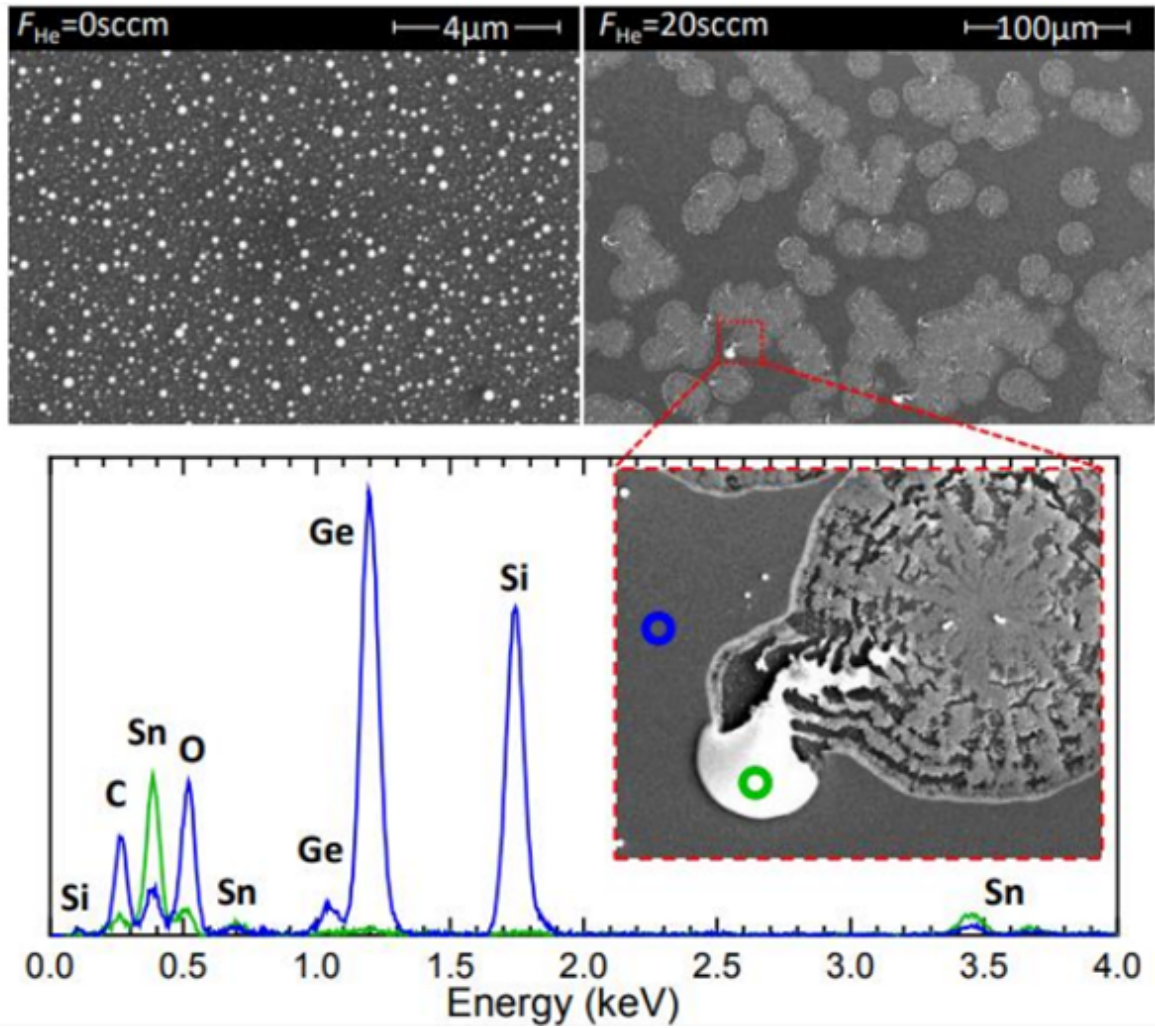
Figure 6.2: SEM images (top) and an EDX spectrum (bottom) of the top-right a-GeSn:H film. The helium flow is 0sccm in the top-left image and 20sccm in the top-right image. Both films have a δ of 100. The green EDX spectrum corresponds to the tin cluster, whereas the blue spectrum corresponds to the background surface. The blue and green circles show where the measurements were taken.[34]

photoresponses are found at low δ.

As shown in figure 6.2 (top-left), the tin is deposited in clusters. It was attempted to dilute the TMT with helium before injecting it into the deposition chamber in order to prevent this clustering. However, adding helium did not prevent clustering as seen in figure 6.2 (top-right). It did change the structure of the clusters. Perhaps using a lower δ and different helium flow rates prevents the formation of clusters more effectively.

6.2. Helium Dilution
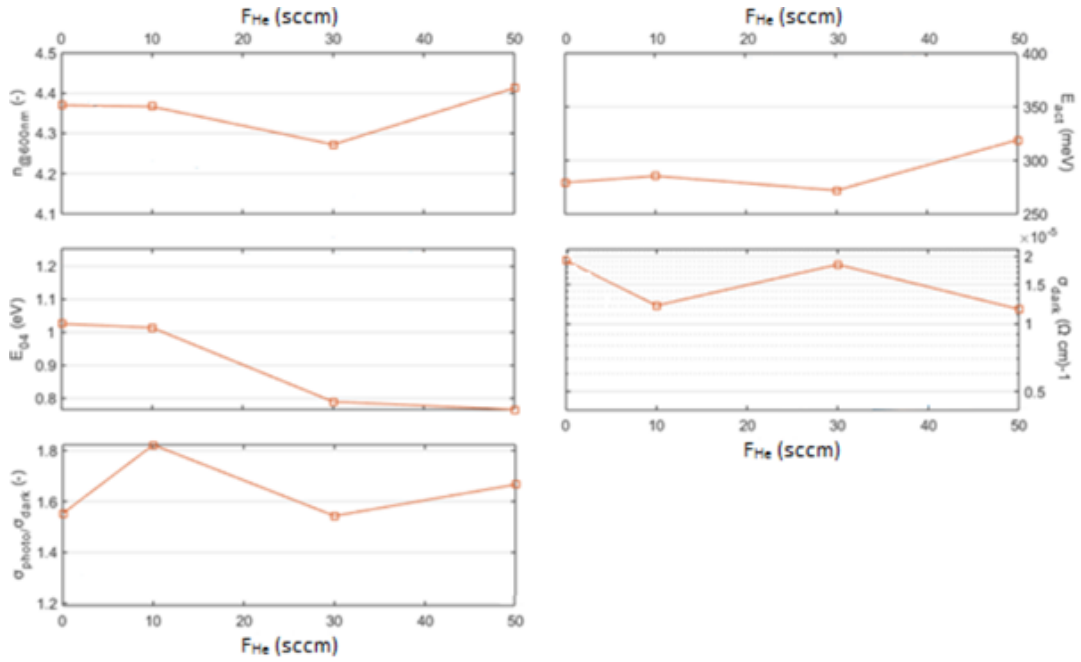
Figure 6.3: Results of varying the helium flow. The deposition conditions for this series can be found in appendix B.3. [34]

Another way to influence the properties of the GeSn:H film is to dilute the TMT with helium before it enters the deposition chamber. In this series, the helium flow is set to 0 sccm, 10 sccm, 30 sccm and 50 sccm.

Figure 6.3 indicates that varying the helium flow into the deposition chamber has very little effect on most parameters. The refractive index remains stable around 4.3-4.4, the activation energy stays around 300 meV, the dark conductivity fluctuates between 1 and 2 $(\Omega cm)^{-1}$ and the photoresponse fluctuates between 1.5-1.8. However, the helium flow has a significant impact on the optical bandgap energy.

The optical bandgap energy decreases sharply with increasing helium flow. It reduces from 1eV to 0.77eV at 50sccm helium flow. This is the lowest measured bandgap of all GeSn:H samples. This finding is very interesting given that the goal is to use GeSn:H as a low bandgap material for bottom junctions in MJ devices. The significantly higher activation energy at 50 sccm helium flow is also beneficial in this regard. All in all, these results suggest that it is beneficial to dilute the TMT flow with helium. However, diluting the TMT injection with helium reduces the amount of carbon in the deposition chamber and because carbon passivates dangling germanium bonds, one would expect $n_{@600nm}$ and E_{act} to decrease with increasing helium dilution rather than increase.
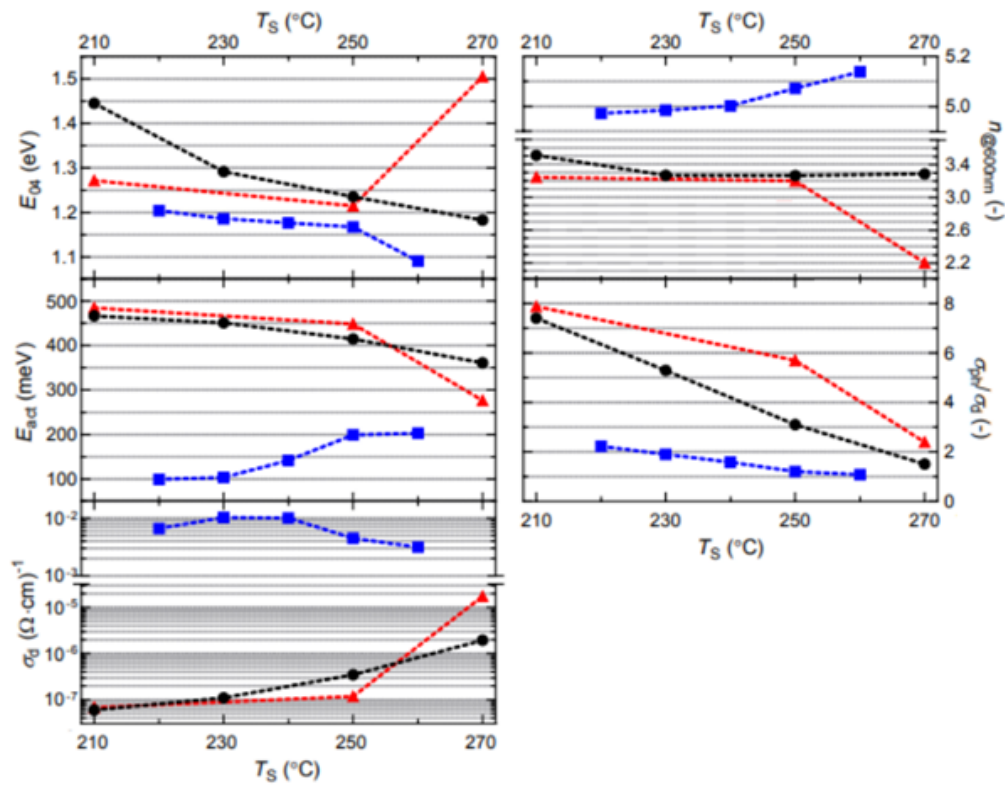
Figure 6.4: Results of varying the temperature in the deposition chamber. The color of each line corresponds to the deposition conditions of the same colour series in appendix B.2. [34]

6.3. Temperature

All results of the blue series in figure 6.4 differ significantly from the other two. The duty cycle of the blue series is 3333, eight times as high as those of the black and red series at 429. The red and black series seem to behave very similarly on all measures. This implies that the omission or inclusion of a 10 sccm helium flow does not have a significant impact on the films.

The bandgap energy has a downward trend with increasing temperatures. The series with 10sccm helium flow has a significantly higher E_{04} at 270°C. For an intrinsic undoped, material a change in E_{04} should result in a change in E_{act} that is twice as large. In other words, $\Delta E_{act} = 0.5 \Delta E_{04}$. This is not the case with the results shown in figure 6.4, where a 200-300meV ΔE_{act} between the low and high δ films corresponds to a mere 100-150meV ΔE_{04}. In general, the films with a low δ have an E_{act} to E_{04} ratio that is closer to 0.5 than the high δ film, which suggests that a higher TMT injection results in films that are closer to device quality. A possible reason for this is that the increased amount of carbon that is injected into the deposition chamber passivates defects in the germanium. This is reflected in the lower dark conductivity and higher photoresponse of the films with a low duty cycle.

The refractive index of the black and red series seem to be independent to changes in temperature, remaining around 3.3. The blue series with the higher δ has a significantly higher refractive index, around 5, which increases further as the chamber temperature increases. This indicates that the film becomes less porous as the deposition temperature increases, because porous material growth leads to a low refractive index. A porous film is also more prone to oxidation, which is makes producing chemically stable a-GeSn:H films unfeasible. The fact that the blue series has a much higher refractive index than the red and black series is in line with the results of the TMT flow experiment. The refractive index of all TMT flow series increases with increasing δ.

All series show a significantly decreasing trend of photoresponse. This suggests that the photocon-ductvitity of the samples become worse as the processing temperature increases. The dark conductivity

is lower for the two low δ series and high for the high δ series. It also increases with increasing temperatures for the low δ series. The high δ series does not show the same trend. Instead, it seems to vary slightly around 10^{-2} $(\Omega cm)^{-1}$.

6.4. Germane Flow Rate
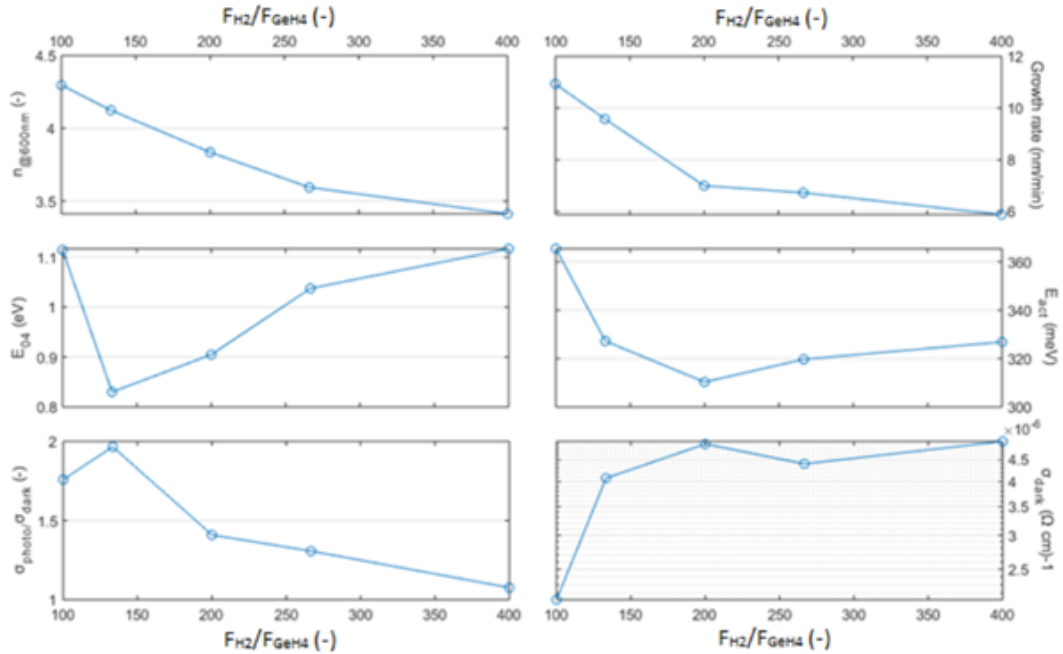
Figure 6.5: Results of varying the germane flow. The deposition conditions for this series can be found in appendix B.3. [34]

The germane (GeH$_4$) flow rate is set to these values in this series: 0.5 sccm, 0.75 sccm, 1 sccm, 1.5 sccm and 2 sccm. These values correspond to a hydrogen dilution ratio (F_{H_2}/F_{GeH_4}) of 400, 266.6, 200, 133.3 and 100 respectively.

Decreasing the germane flow rate results in more porous films, which is reflected in the refractive index in figure 6.5 which decreases steadily with increasing F_{H_2}/F_{GeH_4} ratio. Increasing the germane flow increases the growth rate as indicated by the steadily decreasing growth rate with increasing F_{H_2}/F_{GeH_4} ratio shown in figure 6.5.

The bandgap shows interesting behaviour, dropping from 1.1eV to 0.83eV before slowly increasing back up to 1.1eV again. It is possible that the data point at 2 sccm germane flow rate is an outlier and that the general trend is one of increasing bandgap energy with decreasing germane flow rate. The activation energy decreases rapidly between 100-200 F_{H_2}/F_{GeH_4}, after which it levels off. This suggests that a higher germane flow rate results in films with a lower defect density. The dark conductivity increases slightly between 100-133.3 F_{H_2}/F_{GeH_4}, after which it levels off. The germane flow rate does not seem to have an impact on the dark conductivity.

The photoresponse decreases with increasing F_{H_2}/F_{GeH_4} ratio. This implies that the photoconductivity decreases as well, considering that the dark conductivity stays constant after its initial increase. These are promising results, suggesting that increasing the amount of germanium in the sample increases its photoresponse. All in all, all metrics point in the direction that a high germane flow rate is preferable over a low flow rate to process device quality films. A higher photoresponse increases the current density in the film, a low bandgap is desirable, the material is almost intrinsic due to the ratio of activation energy to bandgap energy, a high growth rate for efficiency and a dense film tin a low porosity and a low defect density are all good qualities for GeSn:H films in PV devices.

6.5. Pressure and Power
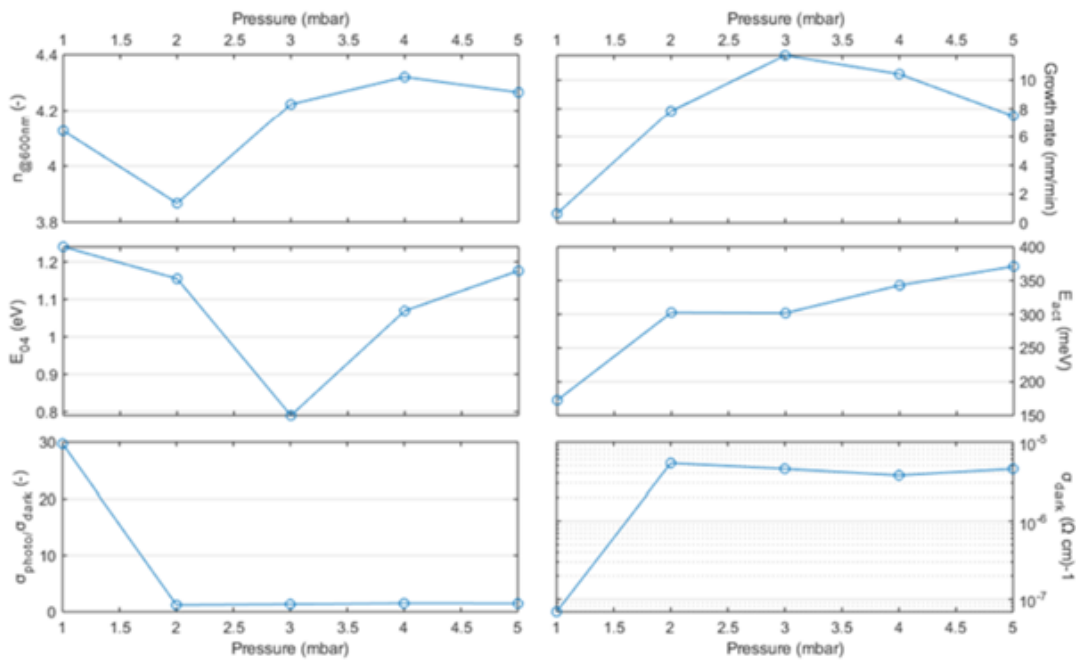
Figure 6.6: Results of varying the pressure. The deposition conditions for this series can be found in appendix B.3. [34]

In the series shown in figure 6.6, the pressure is varied between 1mbar, 2mbar, 3mbar, 4mbar and 5mbar. At 1mbar, the growth rate is more than a factor of 10 lower than at all other pressures in this series. This resulted in a film thickness of 5nm, which is significantly lower than the 50-100nm range that this research has been focused on. At 5nm, the material properties are very different than at 50-100nm. Therefore, the 1mbar results will not be taken into account.

Increasing pressure results in denser films that grow faster, up to a point, indicated by $n_{@600nm}$ and the growth rate in figure 6.6. This suggests that a pressure below 3mbar is suboptimal for processing device quality films, as this results in porous films that also grow slowly.

Increasing pressure results in more chemically stable films, which is indicated by the reducing amount of post-processing oxidation that occurs in the films produced at high pressure. The oxygen concentration decreases steadily with increasing pressure, which is reflected in the increasing E_{act} in figure 6.6. Given that oxidation is undesirable, it is beneficial to learn that it is possible to exert some control on the amount of oxidation in GeSn:H films through changes in pressure.

The power is varied between 3W, 4W, 6W, 8W and 10W in the results shown in figure 6.7. The growth rate increases with increasing power, because higher power increases the dissociation rate in the plasma [5]. Lower powers resulted in denser films, which is reflected in the higher refractive indices. The higher activation energies at 3W and 4W indicate lower defect densities at these power levels. The dark conductivity stays constant excepting the sample at 6W. The photo response has a decreasing trend with increasing power.

There is a trade-off between growth rate and material structure quality when varying the radiofrequency power. Low power is beneficial for the quality, resulting in dense, relatively defect-free films that also have a low bandgap and are capable of generating a high current density. These qualities are indicated by the refractive index, activation energy, E_{04} and photoresponse respectively. However, the films at high power (8-10W) grow around twice as fast as the lower power (3-4W) films.
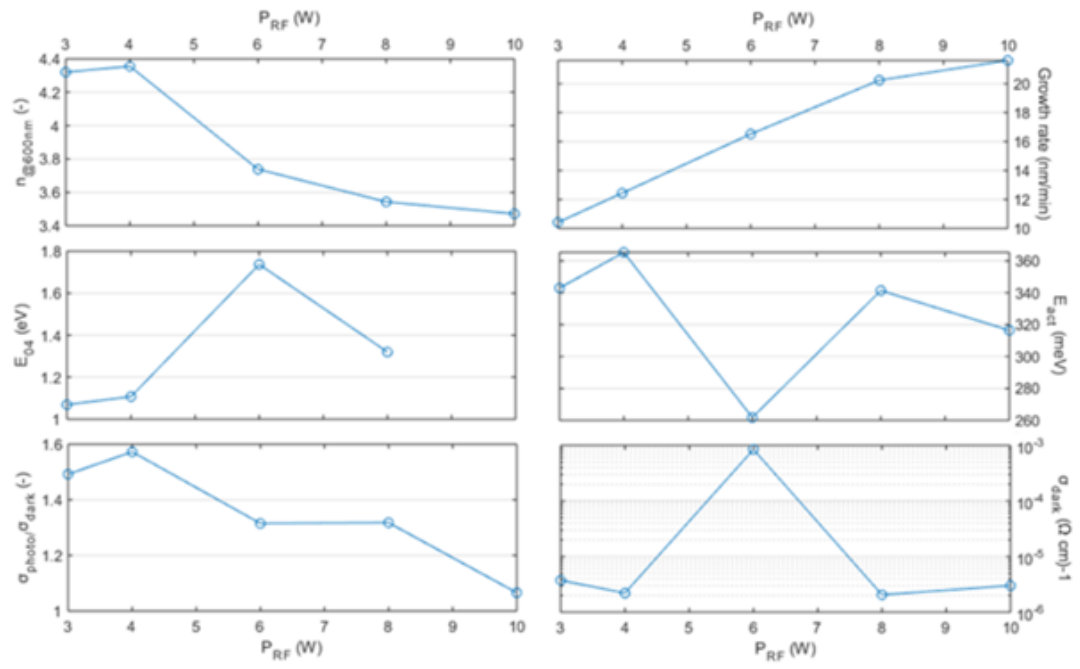
Figure 6.7: Results of varying the power. The deposition conditions for this series can be found in appendix B.3. [34]

7

Conclusions and Recommendations

In this chapter, the conclusions of this research are presented. First, the conclusions and recommendations about the MJ results are discussed followed by the conclusions and recommendations about the GeSn:H results.

Varying the nc-Si middle junction thickness is an effective way to adjust the current densities in the bottom and middle junctions of a c-Si/nc-Si/a-Si PV device. An nc-Si middle absorber thickness range between 3-5µm balances the trade-offs between J_{sc}, V_{oc} and FF. Below 3µm, the nc-Si absorber is too thin to generate an adequate amount of electron-hole pairs, resulting in a J_{sc} that is current limiting. This limits the conversion efficiency of the device. Above 5µm, electrical losses in V_{oc} and FF outweigh the diminishing gains on J_{sc}.

Varying the thickness of the n-nc-SiO$_x$ layer, placed between the n-a-Si and n-nc-Si layers at the bottom of the nc-Si middle junction, is another way to effectively adjust the J_{sc} of the bottom and middle junctions in a c-Si/nc-Si/a-Si PV device. The SiO$_x$ layer functions as an IRL, reflecting light back into the middle junction. The results showed that, in a 20-80nm SiO$_x$ thickness range, increasing the SiO$_x$ thickness increased the J_{sc} of the middle junction at the cost of J_{sc} in the bottom junction. Between 30-80nm, 1.7 mA/cm^2 was lost in the bottom junction while 0.7 mA/cm^2 was gained in the middle junction. Considering that the bottom junction J_{sc} remains nearly twice as high as the middle junction J_{sc}, this is a worthwhile trade-off.

Silver proved ineffective as IRL between the bottom and middle junctions. The bottom junction J_{sc} decreased by 6.3 mA/cm^2 when the Ag thickness was increased from 0-8nm. This large decrease was accompanied by only a 0.1 mA/cm^2 increase in the middle junction and 0.3 mA/cm^2 increase in the top junction. Though the FF was 0.01 higher with a 4nm Ag layer than without, this slight improvement does not warrant the inclusion of a relatively expensive silver layer which is processed in a separate machine adding processing time and complexity.

Introducing TCOs between the n-layer of the middle junction and the p-layer of the bottom junction in c-Si/nc-Si/a-Si devices severely decreased their shunt resistance, which resulted in worse V_{oc} and FF, as well as lower J_{sc} in the middle (current limiting) junction. Even when the measured cells were physically isolated from each other through the use of scribing with a diamond pen or using masks during deposition, the shunt resistance remained orders of magnitude lower in the devices with a TCO in the TRJ between the bottom and middle junctions than in the devices without such a TCO. TCOs should therefore not be used as IRLs in these device architectures.

Finally, the best performing device was manufactured using a 400nm a-Si:H absorber, a 4.5µm i-nc-Si:H absorber and a 60nm SiO$_x$ IRL. The device had a V_{oc} of 1.947V, FF of 0.789, a J_{sc} of 9.51mA/cm^2 and an efficiency of 14.6%.

Carbonization of GeSn:H films due to TMT injections has a major impact on the material structure of said films. Carbon passivates dangling Ge bonds better than hydrogen does which reduces defect density, leading to increased E_{act} at higher TMT injection rates for a-GeSn:H films. However, higher TMT injection rates also lead to more porous, chemically unstable films which oxidize post-processing as indicated by a decreasing refractive index for higher TMT injection rates. Furthermore, higher TMT injection rates result in a material that is more intrinsic as indicated by E_{act} values that are close to half of E_{04}.

Increasing the helium flow to dilute the TMT flow before it enters the deposition chamber results in significantly lower bandgap energies. The film with the lowest bandgap was produced with a helium flow of 50sccm (0.77 eV). Higher deposition temperatures lead to denser films resulting in a higher refractive index.

A high germane flow rate is beneficial for the quality of the processed films and is therefore recommended for future research. A high germane flow rate results in dense, relatively defect-free films with a high photoconductivity, low bandgap and near intrinsic semiconductor properties. These material properties are reflected in the measurements of a lower bandgap, as well as an increased refractive index, growth rate, photoconductivity activation energy.

It is possible to exert control over the amount of oxidation that occurs post-processing by varying the pressure. High pressure resulted in lower oxygen concentrations, which was reflected in the increasing E_{act} values for increasing pressure. Changing the power seems to result in a trade-off between growth rate and film quality, where lower power depositions (3-4W) result in denser, more defect-free films with low bandgaps and a high current density that grow almost twice as slow as the high power depositions (8-10W).

Using a pressure of 3mbar seemed optimal with regards to growth rate. Increasing the power increases the growth rate. However, low power (3-4W) is preferable in terms of bandgap, activation energy, refractive index and photoconductivity. Therefore, it may be worthwhile to sacrifice deposition time (growth rate) in favor of film quality.

A
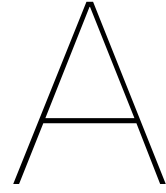
Deposition Conditions for MJ Results

Table A.1: Deposition conditions for the PECVD depositions in AMIGO, ordered from bottom to top. All times and thicknesses that say 'varied' are varied in this thesis.

Layer	DPC #	Temp (°C)	SiH$_4$	H$_2$	CO$_2$	B$_2$H$_6$	PH$_3$	Pressure (µbar)	Power (W)	Time (s)	Thickness (nm)
					Gas flow (sccm)						
SHJ n-side											
n-a-Si	2	300	40				11	0.6	4	86	4
i-a-Si	3	273	40					0.7	3	76	10
SHJ p-side											
i-a-Si	3	273	10	30				1.4	3	75	10
HPT	1	300		200				2.2	9	120	-
i-nc-Si	4	200/170	1.2	120				4	13	120	2-3
p-nc-SiO$_x$	1	300	0.8	170	2.2	10		2.2	12	560	18
p-nc-Si	1	300	0.8	170	170		40	2.2	12	238	3-5
HPT	1	300		200				1.2	8	30	-
nc-Si middle cell											
n-nc-Si	2	300	1	120			2	1.5	11	373	5
n-nc-SiO$_x$	2	300	1	120	1.6		2	1.5	11	varied	varied
n-a-Si	2	300	40				11	0.6	4	168	5-10
HPT	2	300		200				1.2	8	120	-
i-nc-Si	4	200/170	1.2	120				4	40	350	(seed)
i-nc-Si	4	200/170	3.3	120				4	40	varied	varied
i-nc-SiO$_x$	1	300	0.8	170	1.6			2.2	12	60	2-3
p-nc-SiO$_x$	1	300	0.8	170	2.2	10		2.2	12	350	12
p-nc-SiO$_x$	1	300	0.8	170	2.2	50		2.2	12	240	4
HPT	1	300		200				1.2	8	30	-
a-Si top cell											
n-nc-Si	2	300	1	120			2	1.5	11	373	5
n-nc-SiO$_x$	2	300	1	120	1.6		2	1.5	11	1800	30
n-a-Si	2	300	40				11	0.6	4	168	5-10
HPT	2	300		200				1.2	8	120	-
i-a-Si	3	200	2	200				10	9	varied	varied
i-nc-Si	1	300	0.8	170				2.2	35	120	2-3
p-nc-SiO$_x$	1	300	0.8	170	1.8	25		2.2	12	550	2-3
p-nc-Si	1	300	0.8	170		20		2.2	35	70	2-3
HPT	1	300		200				1.2	8	30	-

Table A.2: Deposition parameters for the sputtering processes

Layer	Tool	DPC #	Temperature (°C)	Ar (sccm)	1% O$_2$ (sccm)	Pressure (µbar)	Power (W)	Time (s)	Thickness (nm)
AZO	AMIGO	6	200	20	0	2.6	200	100	15
ITO	ZORRO	2	300	20	0	3.2	60	4108	75
IWO	ZORRO	1	25	15	20	4.0	40	3740	75

Table A.3: Deposition parameters for evaporation processes

Layer	Tool	Evaporation method	Deposition rate (nm/s)	Thickness (nm)
Ag	PROVAC	Resistive heating	0.1	Varied
Cr	PROVAC	E-beam	0.1	30
Al	PROVAC	E-beam	1	500/800

B

CASCADE Deposition Conditions for GeSn:H Samples

B.1. Duty cycle series

Table B.1: Deposition conditions for the TMT flow injection series. F_x represents the flow of the respective gas in sccm. e_d is the distance between the positive and negative electrodes in the deposition chamber.

Series	a-GeSn:H			nc-GeSn:H
	Blue	Purple	Red	Yellow
F_{H_2} (sccm)	200	200	200	200
F_{GeH_4} (sccm)	2	2	2	1
F_{H_2}/F_{GeH_4} (-)	100	100	100	200
F_{He} (sccm)	5	5	5	5
Open time (ms)	7	5-8	7	7
Close time (ms)	5,000-50,000	20,000	5,000-50,000	5,000-40,000
δ(-)	714-7,143	2,500-4,000	714-7,143	714-5,714
Pressure (mbar)	4	4	4	1
Power (W)	3	3	3	5
Temperature (°C)	210	230	270	290
e_d (mm)	11.5	11.5	11.5	13.5

B.2. Temperature series

Table B.2: Deposition conditions for the temperature series

Series	Temperature		
	Black	Red	Blue
F_{H_2} (sccm)	200	200	200
F_{GeH_4} (sccm)	2	2	2
F_{H_2}/F_{GeH_4} (-)	100	100	100
F_{He} (sccm)	0	10	5
Open time (ms)	7	7	6
Close time (ms)	3,000	3,000	20,000
δ(-)	429	429	3333
Pressure (mbar)	4	4	4
Power (W)	3	3	3
Temperature (°C)	210-270	210-270	220-260
e_d (mm)	11.5	11.5	11.5

B.3. Remaining series

Table B.3: Deposition conditions for the helium dilution, germane flow, pressure, and power series

Series	Helium dilution	Germane flow	Pressure	Power
F_{H_2} (sccm)	200	200	200	200
F_{GeH_4} (sccm)	2	varied	2	2
F_{H_2}/F_{GeH_4} (-)	100	varied	100	200
F_{He} (sccm)	varied	5	5	5
Open time (ms)	7	7	7	7
Close time (ms)	20,000	20,000	20,000	20,000
δ(-)	2,857	2,857	2,857	2,857
Pressure (mbar)	4	4	varied	4
Power (W)	3	3	3	varied
Temperature (°C)	270	230	230	230
e_d (mm)	11.5	11.5	11.5	11.5

Bibliography

[1] *Amorphous silicon*. Apr. 2022. URL: `https://en.wikipedia.org/wiki/Amorphous_silicon`.

[2] Rainer Behrisch and K Wittmaack. *Sputtering by particle bombardment*. Vol. 1. Springer-Verlag New York, 1981.

[3] Ashish Binani. "Optimizing the p-contact of nip substrate solar cell: for multi-junction device". In: (2019).

[4] J.W. Bishop. "Computer simulation of the effects of electrical mismatches in photovoltaic cell interconnection circuits". In: *Solar Cells* 25.1 (1988), pp. 73–89. ISSN: 0379-6787. DOI: `https://doi.org/10.1016/0379-6787(88)90059-2`. URL: `https://www.sciencedirect.com/science/article/pii/0379678788900592`.

[5] Bilal Bouazzata. "Development of a-/nc-Ge:H - Growth and characterization of a low bandgap material". In: (2020).

[6] P. Buehlmann et al. "In situ silicon oxide based intermediate reflector for thin-film silicon micromorph solar cells". In: *Applied Physics Letters* 91.14 (2007), p. 143505. DOI: `10.1063/1.2794423`. eprint: `https://doi.org/10.1063/1.2794423`. URL: `https://doi.org/10.1063/1.2794423`.

[7] P. Chatterjee and P. Roca i Cabarrocas. "Influence of N-type μc-SiOx:H intermediate reflector and top cell material properties on the electrical performance of "micromorph" tandem solar cells". In: *AIP Advances* 8.1 (2018), p. 015115. DOI: `10.1063/1.5005114`. eprint: `https://doi.org/10.1063/1.5005114`. URL: `https://doi.org/10.1063/1.5005114`.

[8] *Cost of Energy (LCOE)*. Oct. 2020. URL: `http://trinomics.eu/wp-content/uploads/2020/11/Final-Report-Cost-of-Energy-LCOE.pdf`.

[9] *Data & Statistics*. 2020. URL: `https://www.iea.org/data-and-statistics/data-browser?country=WORLD&fuel=Energy+consumption&indicator=TFCbySource`.

[10] Thierry de Vrijer et al. "PECVD Processing of low bandgap-energy amorphous hydrogenated germanium-tin (a-GeSn:H) films for opto-electronic applications". In: *Applied Materials Today* 27 (2022), p. 101450. ISSN: 2352-9407. DOI: `https://doi.org/10.1016/j.apmt.2022.101450`. URL: `https://www.sciencedirect.com/science/article/pii/S2352940722000890`.

[11] Thierry de Vrijer et al. "The fundamental operation mechanisms of nc-SiOX≥0:H based tunnel recombination junctions revealed". In: *Solar Energy Materials and Solar Cells* 236 (2022), p. 111501. ISSN: 0927-0248. DOI: `https://doi.org/10.1016/j.solmat.2021.111501`. URL: `https://www.sciencedirect.com/science/article/pii/S0927024821005390`.

[12] Mohammed El Makkaoui. "Effect of Pore Size and Distribution on the PEC Properties of Si-Based Porous Monolithic Water-Splitting Devices". In: (2020).

[13] Inc. Filmetrics. *Refractive index of Ge, germanium*. URL: `https://www.filmetrics.com/refractive-index-database/Ge/Germanium`.

[14] Inc. Filmetrics. *Refractive index of Si, silicon*. URL: `https://www.filmetrics.com/refractive-index-database/Si/Silicon`.

[15] Inc. Filmetrics. *Refractive index of Sn, tin*. URL: `https://www.filmetrics.com/refractive-index-database/Sn/Tin`.

[16] Jordan Hanania, Kailyn Stenhouse, and Jason Donev. *Band gap*. Nov. 2015. URL: `https://energyeducation.ca/encyclopedia/Band_gap`.

[17] K W Harrison et al. "Hydrogen Production: Fundamentals and Case Study Summaries; Preprint". In: (Jan. 2010). URL: `https://www.osti.gov/biblio/971440`.

[18] Christiana Honsberg and Stuart Bowden. *IV curve*. URL: `https://www.pveducation.org/pvcdrom/solar-cell-operation/iv-curve`.

[19] Jingya Hou et al. "An examination of the 'tunnel junctions' in triple junction a-Si:H based solar cells: modeling and effects on performance". In: *The Conference Record of the Twenty-Second IEEE Photovoltaic Specialists Conference - 1991* (1991), 1260–1264 vol.2.

[20] Ammar Al-Husseini and Bashar Lahlouh. "Influence of pyramid size on reflectivity of silicon surfaces textured using an alkaline etchant". In: *Bulletin of Materials Science* 42 (May 2019), p. 152. DOI: `10.1007/s12034-019-1848-7`.

[21] E. Kasper et al. "Germanium tin: silicon photonics toward the mid-infrared". In: *Photonics Research* 1.2 (Aug. 2013), pp. 69–76. DOI: `10.1364/PRJ.1.000069`. URL: `http://opg.optica.org/prj/abstract.cfm?URI=prj-1-2-69`.

[22] Simon Kirner et al. "Wafer Surface Tuning for a-Si:H/μc-Si:H/c-Si Triple Junction Solar Cells for Application in Water Splitting". In: *Energy Procedia* 102 (Dec. 2016), pp. 126–135. DOI: `10.1016/j.egypro.2016.11.327`.

[23] Charles Kittel. "Semiconductor Crystals". In: *Introduction to Solid State Physics*. 8th ed. John Wiley & Sons, Inc, 2005, p. 190.

[24] R. H. Klazes et al. "Determination of the optical bandgap of amorphous silicon". In: *Philosophical Magazine B* 45.4 (1982), pp. 377–383. DOI: `10.1080/01418638208227445`. eprint: `https://doi.org/10.1080/01418638208227445`. URL: `https://doi.org/10.1080/01418638208227445`.

[25] Libretexts. *Number of vibrational modes in a molecule*. Apr. 2022. URL: `https://chem.libretexts.org/Bookshelves/Physical_and_Theoretical_Chemistry_Textbook_Maps/Supplemental_Modules_(Physical_and_Theoretical_Chemistry)/Spectroscopy/Vibrational_Spectroscopy/Vibrational_Modes/Number_of_Vibrational_Modes_in_a_Molecule`.

[26] Rebecca Lindsey. Aug. 2020. URL: `https://www.climate.gov/news-features/understanding-climate/climate-change-atmospheric-carbon-dioxide`.

[27] Sander Miedema. "Improved current matching in all-silicon triple-junction solar cells for wireless photo-electrochemical devices". In: (2021).

[28] David A. van Nijen. "Development of a c-Si/nc-Si:H/a-Si:H multi-junction device with a smooth c-Si surface texture". In: (2020).

[29] H. Parasramka. "Design of multijunction solar cells based on thin film silicon". In: (2020).

[30] Paula Perez-Rodriguez et al. "Designing a hybrid thin-film/wafer silicon triple photovoltaic junction for solar water splitting". In: *Progress in Photovoltaics: Research and Applications* 27.3 (2019), pp. 245–254. DOI: `https://doi.org/10.1002/pip.3085`. URL: `https://onlinelibrary.wiley.com/doi/abs/10.1002/pip.3085`.

[31] *PN-junction*. Jan. 2022. URL: `https://wanda.fiu.edu/boeglinw/courses/Modern_lab_manual3/pn_junction.html`.

[32] Armin Richter, Martin Hermle, and Stefan W. Glunz. "Reassessment of the Limiting Efficiency for Crystalline Silicon Solar Cells". In: *IEEE Journal of Photovoltaics* (July 2013). DOI: `DOI:10.1109/JPHOTOV.2013.2270351`.

[33] Steven Roerink. "Development of a-SiGe:H from material characterization to multi-junction device". In: (2019).

[34] Koos Roodenburg. "Development of the low bandgap materials Ge:H and GeSn:H by plasma enhanced chemical vapor deposition". In: (2021).

[35] Sven Rühle. "Tabulated values of the Shockley–Queisser limit for single junction solar cells". In: *Solar Energy* 130 (2016), pp. 139–147. ISSN: 0038-092X. DOI: `https://doi.org/10.1016/j.solener.2016.02.015`. URL: `http://www.sciencedirect.com/science/article/pii/S0038092X16001110`.

[36] Hitoshi (□□) Sai, Kimihiko (□□□□) Saito, and Michio (□□□□) Kondo. "Enhanced photocurrent and conversion efficiency in thin-film microcrystalline silicon solar cells using periodically textured back reflectors with hexagonal dimple arrays". In: *Applied Physics Letters* 101.17 (2012), p. 173901. DOI: `10.1063/1.4761956`. eprint: `https://doi.org/10.1063/1.4761956`. URL: `https://doi.org/10.1063/1.4761956`.

[37] William Shockley and Hans J. Queisser. "Detailed Balance Limit of Efficiency of p-n Junction Solar Cells". In: *Journal of Applied Physics* 32 (Mar. 1961). DOI: `https://doi.org/10.1063/1.1736034`. URL: `https://aip.scitation.org/doi/10.1063/1.1736034`.

[38] *Single diode equivalent circuit models*. URL: `https://pvpmc.sandia.gov/modeling-steps/2-dc-module-iv/diode-equivalent-circuit-models/`.

[39] Arno Smets et al. *Solar Energy. The physics and engineering of photovoltaic conversion technologies and systems*. UIT Cambridge Ltd., 2016.

[40] HF Sterling and RCG Swann. "Chemical vapour deposition promoted by rf discharge". In: *Solid-State Electronics* 8.8 (1965), pp. 653–654.

[41] *Sunlight*. Nov. 2021. URL: `https://en.wikipedia.org/wiki/Sunlight`.

[42] T. Todorov, O. Gunawan, and S. Guha. "A road towards 25% efficiency and beyond: Perovskite tandem solar cells". In: *Molecular Systems Design & Engineering* 1.4 (2016), pp. 370–376. DOI: `10.1039/c6me00041j`.

[43] Thierry de Vrijer et al. "The flexible use of amorphous silicon germanium in thin film silicon multijunction solar cells". In: ().

[44] *What is ellipsometry?* Nov. 2019. URL: `https://www.jawoollam.com/resources/ellipsometry-tutorial/what-is-ellipsometry`.

[45] Maik Wiering. "New Methods of Texturing Crystalline Silicon". In: (2020).

[46] Andrew Zhao. Nov. 2015. URL: `http://large.stanford.edu/courses/2015/ph240/zhao-a1/`.